Simulation of Pressure-Tooling Wire-Coating Flow with Phan-Thien/Tanner Models

V. NGAMARAMVARANGGUL AND M. F. WEBSTER*

Institute of Non-Newtonian Fluid Mechanics,
Department of Computer Science,
University of Wales, Swansea, SA2 8PP, UK.

Int. J. Num. Meth. Fluids, 20th June 2000.

SUMMARY

Annular pressure-tooling extrusion is simulated for a low density polymer melt using a Taylor-Petrov-Galerkin finite element scheme. This represents industrial-scale wire-coating. Viscoelastic fluids are modeled via three forms of Phan-Thien/Tanner (PTT) constitutive laws employed for short-die and full specification pressure-tooling. Effects of variation in Weissenberg number (*We*) and polymeric viscosity are investigated. Particular attention is paid to mesh refinement to predict accurate results. The impact of variation in shear-thinning and strain-softening properties is considered upon the modelling predictions. For the short-die flow, the influence of the lack of strain softening is identified. For the full-die flow and more severe deformation rates, the linear PTT model failed to converge. In contrast, the exponential PTT model is found to be more stable numerically and to adequately reflect the material response. Comparing short-die and full-die pressure-tooling results, shear rates increase ten fold, while strain rates increase hundred times.

1. INTRODUCTION

This study covers the numerical simulation of complex flows, highly viscoelastic in nature, which occur during industrial wire-coating processes. Typically, pressure-tooling and tube-tooling are two distinct die designs applied in the coating process. For thinly coated (narrow-bore) wires, pressure-tooling is employed, where the wire-coating process begins within the die cast. On the other hand, tube-tooling relies on draw-down effects resulting from contact between wire and polymer melt outside the die, to produce thick (wide-bore) cable coatings. This article concentrates on the pressure-tooling design.

Wire-coating, in the pressure-tooling context, constitutes a process of two flow regimes: a shear dominated flow within an annular die, and an extension-dominated flow along the wire-coating region beyond the die. Injection of the molten polymer into the tooling die establishes a pressure driven flow. Contact between the molten plastic tube and the wire is made within the die, where the travelling wire induces a drag flow, drawing out the polymer melt to form a sheath around the cable. Coating production lines for narrow-

* Author for correspondence

bore wire use relatively high speeds, around 1 meter per second, and the deposition of the fluid on a rigid moving wire is treated as a free surface problem. Coverage of this problem, background and the literature is provided below.

In our past work[1] with fixed surfaces, we have adopted differential viscoelastic models, such as the exponential Phan-Thien/Tanner (PTT) model. This permitted us to predict stress development, based upon the recommendations proposed in Binding *et al.*[2] (see section 2, below). There, state-of-the-art finite element (FE) techniques are required to cope with the high deformation rates encountered and associated high Weissenberg numbers, of the order 10^2 to 10^4. Previous predictive methods of this sort are represented in References 3-7. For Newtonian viscous flows, a semi-implicit Taylor-Galerkin/pressure-correction procedure was used by the present authors[8] for solving wire-coating flows, pressure-tooling and tube-tooling, both with and without slip conditions imposed within the die.

With the inclusion of free surfaces, our earlier work on model problems addressed stick-slip and die-swell flows, see References 9-10. There, attention was focused on the effects of drag flow for Newtonian planar and axisymmetric flows[9] and in contrast to the theory. Likewise, a second article[10] extended this work to embrace viscoelastic flows with an Oldroyd-B model representation. Stress stabilisation is performed by invoking a streamline upwind Petrov-Galerkin (SUPG) technique, in conjunction with a recovery method for velocity gradients. The present study goes further in two directions: incorporating more physically realistic constitutive models (PTT) and in addressing industrially relevant pressure-tooling die designs. Free surface schemes are implemented as in References 8-10, to model the extrudate flow. Our aim in this investigation is to provide a comparative study of shear-thinning and strain-softening properties, detecting their respective influence upon the flow fields generated. In this respect, we employ linear, quadratic and exponential PTT models. As a by-product, we are able to isolate the underlying properties that dictate smooth numerical solutions, and those that lead to premature numerical divergence. Flows are analysed under creeping conditions in a two-dimensional annular coordinate setting.

2. BACKGROUND ON WIRE-COATING

Computational and experimental studies are reported widely in the literature for wire-coating flows. In the modelling work, assumptions taken (see Mutlu et al.[5]) include incompressibility for the coating, concentricity of the wire, commonly isothermal conditions and speeds of wire of up to one meter per second. The most popular approach has been to adopt finite element discretisation for two-dimensional annular systems. Both die designs of pressure and tube-tooling are discussed, with emphasis upon pressure-tooling, unless stated otherwise.

Tadmor and Bird[11] (1974) considered the problem of a wire traveling on an axis parallel, but not co-linear to the die. Since the wire was centred with a guider before entering the die, and the wire was under high tension, the problem is more ideal than practical. Their work confirmed that concentricity is restored by the net lateral forces, and this lends to additional justification to a concentric flow assumption.

Recent attention by a number of authors has focused on the numerical simulation of pressure-tooling flow for viscous fluids, such as those of Caswell and Tanner[12],

Pittman and Rashid[13], Mitsoulis[14], Mitsoulis *et al.*[15], and Wagner and Mitsoulis[16]. Their work dealt mainly with shear flow under both isothermal and non-isothermal conditions. Molten polymers have been noted to exhibit highly elastic behaviour when subject to large deformation[11]. Only recently, numerical techniques have proven capable of reaching solutions for sufficiently high and relevant levels of elasticity: limited attempts include those of References 12 and 17. Many other attempts involving either lubrication or inelastic approximations have been conducted to addressed these shortcomings[12,15,18-20].

A whole flow field analysis, regarded as a benchmark in wire-coating analysis, was presented by Caswell and Tanner[12] (1978). This involved an isothermal FE study, without the use of a lubrication approximation. Some interesting findings emerged, including the formation of recirculating regions and the free surface determination at the die-exit. The majority of their analysis dealt with inelastic power-law and Newtonian fluids.

A theoretical and experimental investigation of power-law fluids in the wire-coating process was put forward by Han and Roa[19] (1978). Both tube and pressure-tooling designs were discussed. The wire speeds they used were however, lower than typically, encountered industrially. Increasing wire-speed subsequently effects the reduction of axial pressure gradient and recoverable elastic strain within the molten polymer at the die-exit.

Carley *et al.*[21] (1979) performed a non-isothermal flow analysis for conical and cylindrical dies. Although their energy equation did not include the radial convection term, they were able to model the melt rheology involved reasonably well for a wide range of shear rates.

A high-speed wire-coating study was performed by Chung[22] (1986), obeying the Spencer-Gilmor equation of state. An FE model was used with a lubrication approximation in a cylindrical system. The analysis made apparent the importance of taking material compressibility into account, beyond specific wire speeds, and its effect upon the final wire-coating for power-law fluids. In such a context, the authors advocated care at wire speeds exceeding 0.5 meters per second, with respect to the issue of compressibility.

Mitsoulis[14] (1986) studied the wire-coating flow of power-law and Newtonian fluids. The FE analysis indicated that for realistic predictions, it was necessary to capture the following features in the modelling: normal stresses, temperature-dependent viscosity, and other material properties. Also, Mitsoulis concluded that the inclusion of shear-thinning reduced the (small) levels of die-swell at the die-exit, as well as the recirculation that occurred within the die. In a subsequent article, Mitsoulis *et al.*[15] (1988) provided a detailed numerical investigation into high-speed industrial wire-coating. Two flow formulations were used: a planar FE analysis for non-isothermal flows, and a lubrication approximation for isothermal, power-law fluids. The latter form was found to give the better flow predictions. The non-isothermal pressure solution was found to be in good agreement with the experimental results of Haas and Kewis[23] (1974).

The predictions of Binding *et al.*[2] (1996) made apparent the inadequacy of inelastic models in the accurate modelling of stress and pressure drop throughout the process. These authors made use of inelastic modelling techniques for a pressure-tooling flow, to investigate the mixed extensional-shear flow behaviour of low-density polyethylene melts. A range of viscous models were contrasted, from pure shear models, to mixed and pure extensional models, referencing the stress and pressure fields

generated. Recommendations were made for the accurate prediction of residual stresses in the melt coating, commending a viscoelastic analysis to account for the influence of short residence times of the particles within the flow.

For tube-tooling flows and fixed free-surface estimation, we have conducted single-mode PTT simulations in Mutlu *et al.*[4-5] (1998) and Matallah *et al.*[24] (2000). Using the same Taylor-Galerkin/pressure-correction procedure as identified above, tube-tooling was analysed in sections in Mutlu *et al.*[5], isolating draw-down flow and studying the effects of stress pre-history and various boundary conditions. This led to a further study on coupled and decoupled solution procedures for a range of model fluids, approaching those of industrial relevance. In Matallah *et al.*[24], single-mode model calculations were compared to those of multi-mode type for LDPE and HDPE grade polymers. The multi-mode computations revealed the dominant modes of most significance in the process and gave insight as to the levels of residual stress in the resultant coatings. Further work on multi-mode modelling of Matallah *et al.*[1], emphasised the influence of die-design on optimal process setting. Three, as opposed to seven modes, were found adequate to sufficiently describe the flow. The draw-down residence time, which dictates the dominance of certain modes within the relaxation spectrum, was found to be the primary factor to influence the decay of residual stressing in the coating.

It is upon this basis that we undertake the present study, focusing upon pressure-tooling die-design and the inclusion of free surface movement. Variation in flow response as a consequence of material rheology is of particular interest.

3. GOVERNING EQUATIONS

In this work, Phan-Thien/Tanner models[25-26] are selected for being more physically realistic than say, the constant shear viscosity Oldroyd-B model. The non-dimensional constitutive equation for a generalized PTT model can be written in the general form:

$$We\,\boldsymbol{\tau}_{t} = 2\mu_1 \boldsymbol{D} - f\boldsymbol{\tau} + We\{\boldsymbol{\tau}\cdot\nabla\boldsymbol{U} + (\nabla\boldsymbol{U})^{\dagger}\cdot\boldsymbol{\tau} - \boldsymbol{U}\cdot\nabla\boldsymbol{\tau} + \xi[\,\boldsymbol{D}\cdot\nabla\boldsymbol{\tau} + (\,\boldsymbol{D}\cdot\boldsymbol{\tau})^{\dagger}\,]\}\,, \tag{1}$$

where

$$\boldsymbol{T} = \boldsymbol{\tau} + 2\mu_2 \boldsymbol{D}\,, \tag{2}$$

$$\mu = \mu_1 + \mu_2\,, \tag{3}$$

$$\boldsymbol{D} = \tfrac{1}{2}(\nabla\boldsymbol{U} + \nabla\boldsymbol{U}^{\dagger})\,. \tag{4}$$

Here, $\boldsymbol{\tau}$ is the polymeric component of the extra-stress tensor $\boldsymbol{T}$, $\boldsymbol{D}$ is the rate of deformation tensor, $\boldsymbol{U}$ is the velocity vector, *We* is a Weissenberg number (see below), μ_1 and μ_2 are polymeric and solvent viscosity, superscript † denotes matrix transpose, ∇ is the gradient operator, $\boldsymbol{T}$ is the extra-stress tensor and p is pressure. The function, f, specifies the various versions of this class of models, namely as:

linear model: $$f = 1 + \tfrac{\varepsilon We}{\mu_1}\,trace(\boldsymbol{\tau}) \tag{5}$$

quadratic model: $$f = 1 + \tfrac{\varepsilon We}{\mu_1}\,trace(\boldsymbol{\tau}) + \tfrac{1}{2}\,[\,\tfrac{\varepsilon We}{\mu_1}\,trace(\boldsymbol{\tau})]^2 \tag{6}$$

exponential model: $$f = exp[\,\tfrac{\varepsilon We}{\mu_1}\,trace(\boldsymbol{\tau})] \tag{7}$$

where model parameters $\varepsilon(\varepsilon \geq 0)$ and $\xi(0 \leq \xi \leq 2)$ are non-dimensional characteristic fluid parameters that can be evaluated by fitting to the experimental data. The Oldroyd-B model is recovered when f=1, ε and ξ vanish.

Such PTT model variants may display a wide variety of shear-thinning and strain-softening behaviour. With the above constitutive equation of state (1), we must couple the associated equations for mass conservation and momentum transport to define the governing system. Hence for incompressible, isothermal flow, in the absence of body forces, we have:

$$\nabla \cdot \boldsymbol{U} = 0 \tag{8}$$

$$Re\,\boldsymbol{U}_t = \nabla \cdot \boldsymbol{T} - Re\,\boldsymbol{U} \cdot \nabla \mathbf{U} - \nabla p \tag{9}$$

The complete system is defined via equations (1), (8) and (9).

Non-dimensionalisation of the governing equations requires scales for velocity of U for the wire speed, L for coating length (see Figure 4(b)), $\frac{L}{U}$ for time, $\frac{\mu U}{L}$ for stress and pressure. The viscosity μ is made up of the polymeric viscosity μ_1 (vanishes for Newtonian fluids) and solvent viscosity μ_2, where $\mu=\mu_1+\mu_2$. The non-dimensional Reynolds number is defined as $Re = \frac{\rho UL}{\mu}$, and Weissenberg number as $We = \frac{U\lambda_1}{L}$, where ρ denotes fluid density, and λ_1 an averaged relaxation time.

The PTT models, such as those described by Bird *et al.*[27], are here referred to as PTT (ε,ξ,μ_1). Then, as a special case, the Oldroyd-B model (constant viscosity) is given as PTT (0,0,μ_1). The material parameters that control shear and elongational properties of the fluid are ε (for $\varepsilon \geq 0$) and ξ (where $0 \leq \xi \leq 2$), respectively.

4. NUMERICAL SCHEME

4.1 Discretisation

The system of governing equations for stress, conservation of mass and transport of momentum, as mentioned above (see equations (1), (8) and (9)), with inclusion of appropriate initial and boundary conditions, is solved by a Taylor-Petrov-Galerkin-pressure correction finite element scheme (as commended by Matallah *et al.*[1] and Carew *et al.*[28]). The procedure involves a fractional-staged approach to solve the primary velocity, pressure and stress variables of the system, with incorporation of a time stepping scheme to enable calculation of complex flow stationary solutions in viscoelastic fluids. The time-stepping scheme includes a semi-implicit treatment for the momentum equation to avoid restrictive viscous stability constraints. Solution of each fractional-staged equation is accomplished via an iterative solver. That is, with the exception of the temporal pressure-difference Poisson equation, which is solved through a direct Choleski procedure.

The semi-implicit Taylor-Galerkin/pressure-correction method may be presented in semi-discrete temporal format as:

Stage 1a:

$$\frac{2\,Re}{\Delta t}(\boldsymbol{U}^{n+\frac{1}{2}} - \boldsymbol{U}^{n}) = [\nabla\cdot(2\mu_2\boldsymbol{D} + \tau) - Re\,\boldsymbol{U}\cdot\nabla\boldsymbol{U} - \nabla p]^{n} + \nabla\cdot\mu_2(\boldsymbol{D}^{n+\frac{1}{2}} - \boldsymbol{D}^{n}),$$

$$\frac{2We}{\Delta t}(\tau^{n+\frac{1}{2}} - \tau^{n}) = 2\mu_1\boldsymbol{D} - f\tau - We[\boldsymbol{U}\cdot\nabla\tau - \nabla\boldsymbol{U}\cdot\tau - (\nabla\boldsymbol{U}\cdot\tau)^{\dagger}]^{n}.$$

Stage 1b:

$$\frac{Re}{\Delta t}(\boldsymbol{U}^{*} - \boldsymbol{U}^{n}) = [\nabla\cdot(2\mu_2\boldsymbol{D} - \nabla p]^{n} + [\nabla\cdot\tau - Re\,\boldsymbol{U}\cdot\nabla\boldsymbol{U}]^{n+\frac{1}{2}} + \nabla\cdot\mu_2(\boldsymbol{D}^{*} - \boldsymbol{D}^{n}),$$

$$\frac{We}{\Delta t}(\tau^{n+\frac{1}{2}} - \tau^{n}) = 2\mu_1\boldsymbol{D} - f\tau - We[\boldsymbol{U}\cdot\nabla\tau - \nabla\boldsymbol{U}\cdot\tau - (\nabla\boldsymbol{U}\cdot\tau)^{\dagger}]^{n+\frac{1}{2}}.$$

Stage 2:

$$\frac{\Delta t}{2\,Re}\nabla^{2}(p^{n+1} - p^{n}) = \nabla\cdot\boldsymbol{U}^{*}.$$

Stage 3:

$$\frac{2\,Re}{\Delta t}(\boldsymbol{U}^{n+1} - \boldsymbol{U}^{*}) = -\nabla(p^{n+1} - p^{n}).$$

Above, n is the time step number and $\boldsymbol{U}^{*}$ is a non-solenoidal vector field. The velocity and stress components of Stage 1a are taken for a half time step (i.e., n+$\frac{1}{2}$), while for Stage 1b the $\boldsymbol{U}^{*}$ velocities and stresses are computed over a full time step (n+1). In combination, Stage 1 constitutes a predictor-corrector doublet. This concludes derivation of stress components for a complete time step. Pressure differences over this period are calculated from the Poisson equation (Stage 2), depending upon the intermediate vector field $\boldsymbol{U}^{*}$. Solution of this Poisson equation yields the solenoidal velocity over a full time step, as shown in Stage 3. As reported by Carew *et al.*[28], no gain in stability or accuracy is made by correction of the stress tensor at Stage 3, so this is omitted here also. Spatial discretisation of the domain Ω involves division into N_e elements, viz,

$$\Omega = \sum_{e=1}^{N_e}\Omega^{e}. \tag{10}$$

The piecewise continuous basis functions are defined over two-dimensional triangular elements, with linear interpolation for pressure, and quadratic for velocity and stress:

$$(\tau_{rr},\tau_{rz},\tau_{zz},\tau_{\theta\theta})^{n} = (T_1^{j},T_2^{j},T_3^{j},T_4^{j})^{n}\phi_j,$$

$$(V_r,V_z)^{n} = (U_j,V_j)^{n}\phi_j,$$

$$(p)^{n} = (P_k)^{n}\psi_k.$$

The index k is associated only with vertex nodes, whilst index j relates to both vertex and mid-side nodes.

The SUPG method is employed to cope with the highly elastic, convection dominated nature of the constitutive equations, and to suppress streamwise noise in the discrete solution (Carew *et al.*[28]). The high precision of the solution is maintained by suppressing cross-stream discretisation error through mesh refinement and the use of

multiple Jacobi iterations (see Gunter *et al.*[3]) . Recovery of velocity gradients within the constitutive equation also enhances stability of the system.

Determination of time step (typically $O(10^{-4})$) is made on the basis of a Courant stability constraint for all meshes. More detailed discussion on this scheme can be found in References 10, Gunter *et al.*[3] and Carew *et al.*[28]

4.2 Free surface procedure

To determine the free surface position, we employ a modified iterative free-surface location method in this paper, following a similar approach to that we have used previously for Newtonian problems. In such a manner, the degree of extrudate swell in a viscoelastic die-swell flow may be determined. The following three boundary conditions apply at a free surface, see Crochet *et al.*[29],

$$v_r n_r + v_z n_z = 0, \tag{11}$$

$$t_r n_r + t_z n_z = S\left(\frac{1}{\rho_1} + \frac{1}{\rho_2}\right), \tag{12}$$

$$t_r n_z - t_z n_r = 0, \tag{13}$$

where: S is the surface tension coefficient, v_r is the radial velocity, v_z is the axial velocity, the unit normal vector to the free surface is $\mathbf{n}=(n_r,n_z)$, principal radii of curvature vector is (ρ_1,ρ_2), and surface traction vector is $\mathbf{t}= (t_r,t_z)= \sigma.\ \mathbf{n}$ with Cauchy stress σ.

Conditions (12) and (13) are typically used as boundary conditions for iterative free surface modelling. By calculating the normal velocity from equation (11), the shape of the upper extrudate boundary can be described, as shown in Figure 1(a) for extrudate from a die. The radial distance from the axis of symmetry in the free jet flow is:

$$R(z_2) = R(z_1) + \int_{z_1}^{z_2} \frac{v_r}{v_z} dz\,. \tag{14}$$

In this work, the integral in equation (14) is evaluated by Simpson's quadrature rule, thus providing an estimate of the extrudate shape. The distance from the axis of symmetry, within each element e_i at axial position z, is represented below:

$$R^{e_i}(z_2) = R^{e_i-1}(z_1) + \int_{z} \frac{v_r^{e_i}}{v_z^{e_i}} dz\,, \tag{15}$$

where,

$$\int_{z} \frac{v_r^{e_i}(z)}{v_z^{e_i}(z)} dz = \frac{h}{6}\left[\frac{v_r^{e_i}(iz-2)}{v_z^{e_i}(iz-2)} + 4\frac{v_r^{e_i}(iz-1)}{v_z^{e_i}(iz-1)} + \frac{v_r^{e_i}(iz)}{v_z^{e_i}(iz)}\right], \tag{16}$$

for length of element, $h = z^{iz} - z^{iz-2}$, $e_i = i^{th}$ element, and finite element nodal velocity components $(v_r^{e_i}, v_z^{e_i})(iz)$.

The procedure of solution is as follows. First, the kinematics for a converged Newtonian solution are used as initial conditions with a relaxed stress field and the fixed free-surface problem is solved. Subsequently, the full problem is computed, involving the free surface calculation, where the surface location itself must be determined. Continuation from one particular viscoelastic solution setting to the next is then employed.

Also, we have found it a useful ploy, with respect to stress stabilization for linear PTT modelling for example, to enforce vanishing surface extra stress as a first approximation, to establish a close estimate of the free-surface position. Once located, then surface stress may be relaxed.

To satisfy the zero normal velocity, free surface boundary condition and to compensate for the adjustment of the free surface, the die-exit nodal coordinates must be modified. As a result, the velocity solution at the new surface position must be reprojected from the previous surface position (see Figure 1(b)). This is achieved by selecting two points (r_1,z_1) and (r_2,z_2) for each element at the vertex and mid-side positions. Since the magnitude of the total velocity v_{total} at the boundary is the same for each element:

$$v_{total} = \sqrt{v_r^2 + v_z^2}\,. \tag{17}$$

The angle α, between the horizontal z and the boundary defines the free surface position:

$$\alpha = tan^{-1}\left(\frac{r_2 - r_1}{z_2 - z_1}\right). \tag{18}$$

Lastly, updated values of velocity components v_r' and v_z' are calculated, viz,

$$\begin{aligned} v_r' &= v_{total}\sin(\alpha)\,, \\ v_z' &= v_{total}\cos(\alpha)\,. \end{aligned} \tag{19}$$

5. SHEAR AND ELONGATIONAL BEHAVIOUR OF PTT MODELS

Most non-Newtonian fluids exhibit non-constant viscosity, for example, displaying shear-thinning where the viscosity is a decreasing function of increasing shear rate. This is illustrated in Figures (2) in pure shear. Figure (3) reflects a similar set of plots, but demonstrating the functional dependence of viscosity under increasing strain-rate in pure uniaxial extension. This is termed the elongational or extentional viscosity behaviour. The merits of the PTT model over the Maxwell model are clearly highlighted by Phan-Thien and Tanner[30], noting that, the Maxwellian elongational viscosity goes infinite at finite strain rates. Under the parameter sets identified in this study, linear versions of the PTT model do not display significant strain-softening properties. In contrast, by retaining higher order terms of the Taylor series expansion, this property may be recaptured, with the emergence of quadratic and exponential PTT models.

The shear and extensional viscosity functions, μ_s and μ_e, of the PTT model variants may be expressed as a function of f itself via

$$\mu_s(\dot\gamma) = \mu_2 + \frac{\mu_1 f}{f^2 + \xi(2-\xi)\lambda_1^2\dot\gamma^2}\,, \tag{20}$$

and

$$\mu_e(\dot\varepsilon) = 3\mu_2 + \frac{2\mu_1}{f - 2(1-\xi)\lambda_1\dot\varepsilon} + \frac{\mu_1}{f + (1-\xi)\lambda_1\dot\varepsilon}\,. \tag{21}$$

In pure shear, μ_s for the exponential PTT(1,0,0.88) model is charted for a range of *We*-values, $1 \le We \le 200$, in Figure 2(a). The gradual drop in shear viscosity from a maximum initial zero plateau to a second Newtonian level of -0.9 units is observed at all *We*-values. The only discernable difference in behaviour between *We*-values is the rate of change of shear viscosity over the shear rate range $10^{-3} \le \dot\gamma \le 10^2$. This rate change increases with *We*, so that the most rapid corresponds to *We*=200. Figure 2(b) illustrates the more

rapid drop in shear viscosity with increasing ε-value: this provides greater shear-thinning properties. Such a feature is incorporated in our short-die, pressure-tooling modelling by inclusion of a case where ε=1.

Shear viscosity profiles in Figure 2(c) are plotted for μ_1-values, ranging from 0.88 to 0.995. The remaining parameters are taken as ε=1, ξ=0 and *We*=200. Typical shear-thinning characteristics are observed, where shear viscosity drops from an initial value of zero to a minimum of -2.3 units (for μ_1=0.995). In our finite element computations below, some short-die, pressure-tooling instances are implemented for μ_1=0.99, reflecting increased shear-thinning over μ_1=0.88, as well as enhanced numerical stability of convergence over μ_1=0.995 (further evidence on this issue is given in the results section below). In Figure 2(d) and 3(d), contrast in model variants is displayed. For this purpose, the maximum *We*-value of 200 is chosen with PTT(1,0,0.99), for which the trends in shear viscosity are presented in Figure 2(d). The parabolic drop due to shear-thinning is practically replicated for all PTT models, falling from a first plateau of zero to a second at –2 units. The transition from linear to exponential PTT is reflected in a slightly more rapid drop to the global minimum and second plateau.

Extensional viscosity profiles of Figure 3 adopt the same parameter setting as those for the pure shear plots of Figure 2. For a Newtonian fluid, at low strain rates the elongational viscosity is three times the shear viscosity. Non-Newtonian polymer melts, such as represented by the PTT(ε,0,0.99) model at *We*=200, produce non-monotonic elongational behaviour (see Figure 3(b) for $0.1 \le \varepsilon \le 0.5$, demonstrating strain-hardening at low strain rates prior to strain-softening.

Under variation in *We* and for the same combination of parameters as for Figure 2(a), the elongational viscosity behaviour of Figure 3(a) is shown to adopt an almost identical pattern to the shear viscosity. Elongational viscosity levels are consistently three times larger than those of the shear viscosity. Such rapid decline in viscosity at *We*=200, reflects industrial experience and calibrations (private communication[31]). A single (averaged) relaxation time, λ_1=2 sec, is selected from data typical for this process (see other References 1, 2 and 4). With the associated velocity and length scales chosen, this yields a maximum value of *We*=200. Variation of extensional viscosity with the ε-paramater is charted in Figure 3(b). A number of theoretical investigations[32-34] have attempted to rationalise the build-up in elongational viscosity to a maximum ("strain-hardening behaviour"), followed by a decrease with increasing elongation rate (as observed in Figure 3(b)). Some experimental studies[35-36] have speculated on the notion of "molecular entanglement"[33] to explain this behaviour. We observe such a response in Figure 3(b) at low ε-values for the exponential PTT model. The temporary rise in elongational viscosity (a stretching effect), that occurs at low extension rates prior to tailing off at high extension rates, is associated with the non-linear exponential term of the model. This paper uses the parameter set of μ_1=0.99, ξ=0 and *We*=200, unless specified otherwise. The model with ε=1 is considered an appropriate choice to suit present requirements due to its monotonic strain-softening behaviour.

Corresponding strain-softening behaviour is observed in Figure 3(c) with variation in μ_1. Again, the elongational viscosity is comparable to one-third the shear viscosity in magnitude (see Figure 2(c)). The more appropriate value, to suit present circumstances, corresponds to the model with μ_1=0.99, due to its combination of strain-softening and numerical stability attributes. The marked differences in strain-softening properties for linear, quadratic and exponential PTT(1,0,0.99) models are observed in Figure 3(d). *Only*

relatively mild strain-softening is observed in the case of the linear PTT model with this choice of parameters. The exponential PTT model demonstrates the more extreme strain-softening behaviour, and is called upon to reflect this position in our short-die pressure-tooling work (as one might encounter, say, for an LDPE grade polymer at 230^{o}C).

Under general flow conditions, there is need to record generalized shear and strain-rates, that are defined via flow invariants as, respectively:

$$\dot{\gamma} = 2\sqrt{II_d} \quad \text{and} \quad \dot{\varepsilon} = 3\frac{III_d}{II_d}, \tag{22}$$

where II_d and III_d are the second and third invariants of the rate of strain tensor $\boldsymbol{D}$. Such quantities are represented as

$$II_d = \frac{1}{2} trace(\boldsymbol{D}) = \frac{1}{2}\{(\frac{\partial V_r}{\partial r})^2 + (\frac{\partial V_z}{\partial z})^2 + (\frac{V_r}{r})^2 + \frac{1}{2}(\frac{\partial V_r}{\partial z} + \frac{\partial V_z}{\partial r})^2\}, \tag{23}$$

$$III_d = det(\boldsymbol{D}) = \frac{V_r}{r}\{\frac{\partial V_r}{\partial r}\frac{\partial V_z}{\partial z} - \frac{1}{4}(\frac{\partial V_r}{\partial z} + \frac{\partial V_z}{\partial r})^2\}. \tag{24}$$

6. PROBLEM SPECIFICATION

Two types of flows are studied here, namely, a short-die pressure-tooling flow, and a full-die pressure-tooling instance. The primary aim of the first case is a preliminary investigation into the flow characteristics for pressure-tooling, without the inclusion of the full die complexity. Aspects of particular interest include the interface from pressure-driven shear flow to drawing flow, and the die-exit conditions. There is need to invoke a free surface location technique to resolve the surface position and to examine the effects on the free jet drawing flow (swelling shape and ratio, χ). This drawing flow is responsible for the coating upon the lower moving-wire boundary. Creeping flow conditions (low Reynolds number of 10^{-4}) are invoked for both short and full-die pressure-tooling.

6.1 Short-die, pressure-tooling

Figure 4(a) illustrates the domain of consideration for this short-die annular pressure-tooling flow. Results for such a problem are computed on a relatively fine mesh of 6×24 elements, 637 nodes, 1449 degrees of freedom, with minimum element size of 0.0645 units (Figure 5(a)). Mesh refinement for this flow follows our precursor work[10]. This model problem is comparable to a classical die-swell flow, but also involves an imposed drag flow due to the moving wire and a free jet flow beyond the die. A fully developed pressure-driven annular flow is imposed at the inlet that provides the inlet flow profile boundary conditions. This fixes the flowrate throughout the die, with no-slip conditions pertaining at the die wall. The moving wire at the lower boundary travels at a constant predefined speed. The location of the free jet boundary surface is defined by a streamline, upon which vanishing traction is assumed. A fully developed plug flow prevails at the outlet. The characteristic velocity is taken as the wire speed, the characteristic length is the inlet channel radius (that includes a wire radius of 0.6 units).

A Newtonian and three PTT model variants are implemented, of linear, quadratic and exponential type. Various parameter ranges are investigated with *We* ranging from 1 to 200 (see back to section 5), and μ_1 ranging from 0.88 to 0.995.

6.2 Full-case, pressure-tooling

The domain considered for the complete pressure-tooling flow is represented in Figure 4(b), upon which the meshes of Table 1 (Figure 13) are constructed. This problem subsumes the short-die flow, covering the land region flow (Z_6Z_7) and a short jet flow zone (Z_5Z_6). Here, we have an abrupt contact point between the moving wire and pressure-driven annular flow that occurs at position Z_3 within the die. Wire conditions are assumed to apply at this point (see References 2 and 8). The extruded melt swells at the free boundary region Z_5Z_6, where tractions vanish and the pressure is atmospheric ($\sigma_{nn}=\sigma_{ns}=P=0$). At the upper and lower die walls (Z_1Z_3 and Z_6Z_{10}), no slip applies. A fully developed plug flow travelling with the wire, is imposed at the outflow Z_4Z_5. The lower domain boundary, Z_3Z_4, corresponds to the wire that moves under a predefined wire speed.

Table 1: Full-die; finite element meshes

Mesh	Element	Total element	Total node	DOF
1. Uniform mesh	12×74	1776	3725	8425
2. Biased coarse mesh	6×114	1368	2977	6759
3. Biased medium mesh	10×168	3360	7077	16013
4. Biased fine mesh	15×127	3810	7905	17858

For this case, the characteristic length is selected as the coating length, R_2, and the characteristic velocity is associated with the wire speed, V_{wire}. The die converging angles at Z_3, Z_7 and Z_8 are $\theta(24^o)$, $\phi(17^o)$ and $\alpha(24^o)$, respectively. A wire radius of 0.09 units is taken here, the die length is 3 units, inlet and outlet hydraulic radii at location Z_1Z_{10} and Z_4Z_5 are 0.5 units and 0.2 units, with land length equal to 0.05 units. The polymer melt enters the die geometry with annular velocity profile $V_z(r)$ (see Reference 9). By comparing the analytical and numerical solutions for velocity and stress at the die-exit, the accuracy of the solution may be assessed. For fully developed steady simple shear flow, the applied inlet boundary stresses $\tau_{ij}(r)$, within the annular pressure-driven flow, can be evaluated as:

$$\tau_{rz} = \frac{\mu_1 f\dot{\gamma}}{f^2 + (We\dot{\gamma})^2 \xi(2-\xi)}, \tag{25}$$

$$\tau_{rr} = \frac{-\xi We\dot{\gamma}}{f}\tau_{rz}, \tag{26}$$

$$\tau_{zz} = \frac{(2-\xi)We\dot{\gamma}}{f}\tau_{rz}, \tag{27}$$

where f is the PTT model function of equations (5)-(7). The azithmutal stress at the inlet vanishes. In each model instance, by substituting equations (25)-(27) into the expressions for the PTT functions, equations (5)-(7), the parameter f may be re-expressed in the following form:

linear model: $$f = 1 + \frac{2\varepsilon(We\dot{\gamma})^2(1-\xi)}{f^2 + (We\dot{\gamma})^2\xi(2-\xi)}, \quad (28)$$

quadratic model: $$f = 1 + \frac{2\varepsilon(We\dot{\gamma})^2(1-\xi)}{f^2 + (We\dot{\gamma})^2\xi(2-\xi)} + \frac{1}{2}\left[\frac{2\varepsilon(We\dot{\gamma})^2(1-\xi)}{f^2 + (We\dot{\gamma})^2\xi(2-\xi)}\right]^2, \quad (29)$$

exponential model: $$f = exp\left[\frac{2\varepsilon(We\dot{\gamma})^2(1-\xi)}{f^2 + (We\dot{\gamma})^2\xi(2-\xi)}\right]. \quad (30)$$

In this manner, non-linear algebraic expressions may be derived for the parameter f. Hence, via a Newton iteration, these expressions may be resolved to identify *f* for each model, appropriate for steady simple shear flow. Once f has been determined, inlet stress boundary conditions may then be gathered from equations (25-27).

7. RESULTS AND DISCUSSION

7.1 Short-die, pressure-tooling

Field contours for short-die pressure-tooling are represented in Figures 5(c)-5(j). This short-die case is considered first, as a precursor to a full specification to simplify some of the many difficulties involved and pinpoint a comparative investigation, removing the complexity associated with the die flow itself. The full case will therefore illustrate the influence of the die flow upon the process. For a 288 element mesh (Figure 5(a)), the velocity vector and contour plots, consisting of radial and axial velocity components, are illustrated in Figures 5(b) to 5(d). The adjustment in flow profile from a shear flow to a plug flow is clearly observed; see also Reference 10. A small reduction in pressure of 0.46 units occurs throughout the length of the die (Figure 5(e)), where the die length to exit gap width ratio is of the order 2:1. The pressure drop across the flow in this case reaches 0.46 units, corresponding to that over the die alone, and the minimum pressure of –0.16 units, is observed close to the top surface die-exit. The dramatic increase in shear rate I_2 to 31.35 units at the top die-exit boundary is observed in Figure 5(f), which declines to zero immediately upon entering the jet region (see on). Figure 5(g) reflects the level of extension within the jet flow region, which rises to a maximum $\dot{\varepsilon}$-value of 0.14 units. Such a level is less than 0.05 percent of that due to shear and indicates which ranges of deformation are most relevant for the flow, with respect to Figure 2 and 3. A correspondingly low T_{rr}-value of 0.008 occurs likewise in Figure 5(h). The T_{rz} and T_{zz}-profiles (Figures 5(i), 5(j)) demonstrate peak singularities at the (upper) boundary die-exit region.

In Figure 6, pressure drop (Δp) is charted along the wire, against various parameter settings. Δp for a range of *We* is plotted in Figure 6(a). Linear reductions in pressure before the die-exit are observed, with *We*=200 giving the smallest pressure difference. This peak *We*-value is used in our further studies to suit industrial requirements, as mentioned above. The most extreme level for initial pressure of 40 units corresponds to the Newtonian case (*We*=0): so that, with introduction of shear-thinning, Δp declines, as one would anticipate. Figure 6(b) illustrates the effects of variation in μ_1 on pressure for the exponential PTT model. The trend in the plot with the paramater choice of μ_1=0.99 correlates to the field pressure contours of Figure 5(e). Reduction in μ_1 from 0.99 to 0.88

gives an almost ten fold increase in pressure drop. The three PTT models variants (linear, quadratic, exponential) all give similar pressure profiles over the length of the die and beyond (Figure 6(c)). The exponential PTT variant provides a slightly lower pressure drop than that for the linear model. We conclude that Δp is more sensitive to adjustment in *We* and μ_1, and less so to choice of model.

Table 2: Short-die; exponential PTT(1,0,0.88), solution variation with *We*

Solution variables	*We*=0	*We*=1	*We*=10	*We*=100	*We*=200
I_2 max	28.77	42.05	31.80	29.08	28.90
$\dot{\varepsilon}$ max	0.084	0.368	0.193	0.049	0.048
Δp	39.81	10.89	5.69	4.89	4.84
T_{rz} max	6.834	1.152	0.156	0.020	0.011
T_{zz} max	40.57	3.60	0.51	0.07	0.04
χ	1.039	1.039	1.051	1.045	1.044

In Figure 7, variation in shear rate at the top surface is examined. Figures 7(a)-7(b) correspond to the exponential PTT model. Higher *We*-values suppress the shear rate peaks at the die-exit, values varying from 42.05 units for *We*=1 to 28.9 units for *We*=200. In contrast, decreasing μ_1 from 0.995 to 0.88 achieves a 14% reduction in the shear rate spike (Figure 7(b)). We particularly note the trends of Figures 7(c) for the linear PTT model behaviour on the top surface. This plot suggests that the relatively constant (flat) elongational viscosity behaviour of Figure 3(d) is responsible for the oscillations in shear rate profile at the die-exit region (lack of strain-softening), reaching a peak of 14.4 units. This result clearly demonstrates the looming inadequacies of the linear PTT model to represent such a flow. Considerably smoother and more stable shear rate plots are reproduced with the quadratic and exponential PTT models (Figure 7(d)). Note here, that shear rate peaks are much higher than for the linear model, attaining values of up to 34.0 units for the quadratic PTT model.

Table 3: Short-die; exponential PTT(1,0, μ_1), *We*=200, solution variation with μ_1

Solution variables	μ_1=0.88	μ_1=0.99	μ_1=0.995
I_2 max	28.90	31.35	33.80
$\dot{\varepsilon}$ max	0.048	0.144	0.363
Δp	4.841	0.462	0.263
T_{rz} max	0.011	0.014	0.017
T_{zz} max	0.038	0.041	0.041
χ	1.044	1.054	1.092

The effect of increasing *We* is to lower strain and shear rate peaks, as represented in Table 2 for the exponential PTT model. This table corresponds to the shear rate profiles of Figure 7(a), where models with lower *We* produce higher shear rates at the top surface.

Modification of μ_1, produces the strain and shear rates of Table 3. Increase in μ_1 is seen to increase shear and strain rate maxima, reaching peaks of 33.8 and 0.363 units, respectively, for μ_1=0.995. Across the three PTT models considered, shear rate maxima are of the order 10^2 greater than those in strain rate. Contrasting the quadratic and exponential versions in Table 4, the lower shear rate peak at the die-exit (Figure 7(d)) is provided by the exponential PTT model. This is confirmed in the shear rate profile plots of Figure 7(c). With the exponential PTT model, the strain rate maxima of 0.144 units corresponds to that in the free-jet of Figure 5(g).

Table 4: Short-die; PTT(1,0,0.99), *We*=200, solution variation with model

Solution variables	Linear	Quadratic	Exponential
I_2 max	14.40	33.95	31.35
$\dot{\varepsilon}$ max	0.963	0.372	0.144
Δp	0.613	0.509	0.462
T_{rz} max	0.414	0.153	0.014
T_{zz} max	6.222	0.381	0.041
χ	1.100	1.088	1.054

Figure 8 quantifies plots for shear stress, T_{rz}, with variation in parameters across the *top surface*. T_{rz}-values are shown in Figure 8(a) for a range of *We*. The Newtonian, initially negative level, drops sharply to –25 units just prior to the die-exit, before an even more violent recovery on entry to the free jet region. For *We*=1, a much reduced negative entry flow value of T_{rz}=–1 units applies within the die (shear-thinning effect). For *We≥10*, minor levels of shear stress are generated. In Figure 8(b), higher μ_1-values provoke an increase in peak T_{rz}-values at the jet-entry region and beyond, with larger T_{rz} within the die. Stress levels are low due to the setting, *We* = 200. This behaviour replicates the shear rate patterns of Figure 7(b). Violent oscillations in the linear PTT profiles prior to die-exit (Figure 8(c)) are the result of strain-hardening effects (see Figure 3(d)), with a peak value of 0.41 units at the pre-die exit. The strain-softening behaviour observed in Figure 3(d), stabilises, the T_{rz}-profile for the quadratic and exponential PTT models (Figure 8(d)). *Smooth profiles result and, in this, we are able to distinguish the influence of strain hardening from softening.* The T_{rz} peak is larger for the quadratic case due to the larger shear rates generated (Figure 7(d)). I_2 inlet values in Figure 7(d) for both models are about 8 units. The shear viscosity log-log plots of Figure 2(d), justify the lower initial shear stress of Figure 8(d). In contrast, we plot in Figure 9, T_{rz}-profiles *along the wire*. From our previous work[10], we observed that for Oldroyd models, the effect of the additional component of drag flow, increases values of axial velocity V_z, shear rate I_2, pressure P, radial stress T_{rr} and shear stress T_{rz}; in contrast reducing radial velocity V_r, axial stress T_{zz} and azimutal stress $T_{\theta\theta}$. A much higher die-entry shear stress occurs for the Newtonian case. For the viscoelastic results, the shear stress of Figure 9(a) tends to zero with increasing *We* due to shear-thinning. The shear stress profiles of Figure 9(b) for increasing μ_1, show a larger T_{rz} within the die, adjusting to lower values beyond the die. Levels correspond to the setting of *We*=200. Differences between the shear stress profiles of the various PTT models at the wire are observed in Figure 9(c). These are a consequence of

the near-vanishing shear rate I_2 in the post-die flow, as well as the local elongational influences, see Figure 3(d).

For axial stress profiles, T_{zz}, and variation with *We*, there is little change on the top surface in Figure 10(a). A spike at die-exit occurs in Figure 10(a): this is magnified considerably below *We*=1 as Newtonian conditions are approached. At *We*=200 in Figure 10(b), τ_{zz}-values are low on the top surface and rise marginally with increasing μ_1. The decline at post-die exit follows the kinematics. The free jet is almost a pure extensional flow, so that,

$$T_{zz} - T_{rr} \approx \dot{\varepsilon}\mu_e(\dot{\varepsilon}).$$

Hence, since T_{rr} is relatively small (Figure 5(h)) in contrast to T_{zz}, T_{zz} depends practically upon the strain rate $\dot{\varepsilon}$ (Table 4), which peaks in the free jet region. The T_{zz} maximum of the linear PTT model (Figure 10(c)) is due to the mild strain-softening effects (high μ_e) post-die exit (Figure 3(d)). The exponential PTT T_{zz}-profile is consistently lower than for the quadratic PTT model (Figure 10(d)), which in turn, is lower than that for the linear model. This is due to the lower elongational viscosity (Figure 3(d)) and shear rates sustained (Figure 8(c)) by the exponential PTT, as opposed to the quadratic (or linear) PTT model. Axial stress along the wire (Figure 11(a)) drops with increasing *We* for viscoelastic fluids due to shear thinning effects within the die. The gradual decline in axial stress for all μ_1-values (Figure 11(b)), corresponds to the decrease in pressure (Figure 5(e)) along the die length. The stress levels are low as *We*=200. The larger values of μ_1 shift the T_{zz}-profiles to larger positive values within the die. Variation across the three PTT models is covered in Figure 11(c). This is most noticeable for the linear PTT model, whose peak of 0.32 units is double that of the quadratic case, and ten times greater than that for the exponential PTT instance. Peak values occur for linear PTT just beyond the die, for quadratic PTT just within the die, and barely at all for the exponential PTT model. The position is similar in shear stress.

Die-swell characteristics along the top free surface are presented in Figure 12. For the exponential PTT model, results are plotted for a range of *We*-values in Figure 12(a). The die-swell for *We*=1 is lower due to the inhibiting influence of the shear and elongational effects. Increasing μ_1 is seen to magnify the die-swell, Figure 12(b). This behaviour confirms the observations made previously concerning strain rate (Table 3), shear stress (Figure 8(b)), and axial stress (Figure 10(b)). For Figure 12(c), it is apparent that retention of the higher order terms of the Taylor series expansions in the PTT model, produces a form that reduces the extent of the die-swell. For these three models, swelling projections are influenced by the corresponding strain rates (Table 4), shear stresses (Figures 8(c), 8(d)), and axial stresses (Figures 10(c) and 10(d)) produced.

7.2 Full-die, pressure-tooling

The range of meshes of Figures 13(a)-13(d) is used for the full pressure-tooling simulations. The zonal refinements are outlined in Table 5, with greatest density and bias in the land and die-exit regions. Results are plotted upon the biased fine mesh (Figure 13(d)), unless otherwise specified. With the prior knowledge of the above short-die study, the specific parameters employed in this flow are: $Re=10^{-4}$, *We*=200, μ_1=0.99, ε and ξ are unity and zero, respectively.

The radial and axial velocity line contour plots of Figures 14(a) and 14(b) show rapid acceleration on approach to the die-exit in both velocity components. An intense drop in pressure local to the land region is observed in Figure 14(c), reaching a maximum

pressure drop of 10.17 units. Shear rate I_2 of Figure 14(d), also identifies significant shearing over the land region, reaching a peak of 461.72 units at the die-exit, a fifteen fold increase to that obtained for short-die, pressure-tooling. Strain rates $\dot{\varepsilon}$ in Figure 14(e), are an order of magnitude lower than shear rates, and display peaks at melt-wire contact and die-exit. At the melt-wire contact point, $\dot{\varepsilon}$ increases to 8.37 units. A rapid larger rise occurs in the wire-coating section at die-exit. The second peak in $\dot{\varepsilon}$-profile at the top boundary, characteristic for the full-die, reaches a height of 18.83 units in the post-die exit region. The "shock impact" as the fluid makes contact with the wire is most prominent in the radial, shear and axial stress contour plots of Figures 14(f) to 14(h). Nevertheless, stresses within the die remain small, the greatest axial stress of 0.069 units occurs at the free jet-entry region.

Table 5: Full-die; mesh characteristics, sub-region zones

Sub-region zone	Uniform mesh	Biased coarse mesh	Biased medium mesh	Biased fine mesh
1. inlet die	12×6	6×20	10×35	15×20
2. converging die	12×12	6×25	10×30	15×25
3. coating region	12×24	6×30	10×35	15×30
4. land region	12×8	6×3	10×8	15×5
5. jet region	12×24	6×36	10×60	15×47

From Table 6, maxima in I_2 correspond to the biased fine mesh at the top surface, although there is little difference in solution values between meshes at the wire boundary. Swelling ratio (χ) is increase by about 15% from coarse to finest meshes. This illustrates the importance of sufficient mesh refinement. Mesh refinement has little influence on $\dot{\varepsilon}$ peaks, pressure drop, and stress maxima, the greatest differences O(5%) are observed in pressure drop, with O(1%) variation in other variables.

Table 6: Full-die; exponential PTT(1,0,0.99), *We*=200, solution variation with mesh refinement

Solution variables	Uniform mesh	Biased coarse mesh	Biased medium mesh	Biased fine mesh
I_2 max, Top	209.9	213.0	383.0	461.7
I_2 max, Bot	145.6	139.6	138.7	139.7
$\dot{\varepsilon}$ max	18.73	18.75	18.72	18.83
Δp	10.49	10.09	10.00	10.18
T_{rz} max	0.019	0.022	0.025	0.025
T_{zz} max	0.058	0.064	0.063	0.069
χ	1.087	1.157	1.258	1.215

The pressure along the bottom surface for the exponential PTT model (Figure 15(a)) corresponds to the line contour plot of Figure 14(c). The higher initial die pressure and lower extrudate pressure illustrate the inaccuracies of the uniform mesh in areas of

high activity. The quadratic PTT pressure value within the die (Figure 15(b)) is 5% higher than that for the exponential PTT model, which confirms the behaviour noted in the previous short-die, pressure-tooling results. Pressure difference for the exponential PTT model is twenty two times greater for the full case, above short-die pressure-tooling (comparing with Figure 6(c)). Note that, these drops in pressure, essentially correspond to the same flow zone, that is, over the land-region jet-entry.

Table 7: Full-die; PTT(1,0,0.99), *We*=200, solution variation with model

Solution variables	Quadratic	Exponential
I_2 max, Top	448.9	461.7
I_2 max, Bot	140.4	139.7
$\dot{\varepsilon}$ max	18.76	18.83
Δp	10.60	10.18
T_{rz} max	0.408	0.025
T_{zz} max	1.639	0.069
χ	1.224	1.215

Shear rate along the top and bottom surface gave almost identical shapes for each mesh tested, the only difference being the die-exit peaks. Hence, shear rate profiles are represented here for the fine mesh only in Figure 16. The top surface I_2 peak of 461.7 units at the die-exit (Figure 16(a)) is fifteen times greater than that for short-die, pressure-tooling (see Figure 7(d)). Further data on I_2 maxima may be found in Tables 6 and 7. Results for the linear PTT model are omitted from Table 7 because it was not possible to gather stable solutions for this model under such high shear and strain conditions, with such large *We*-values. The double (sudden shock) peaks of 124 and 140 units at the bottom surface of Figure 16(b), correspond to the contours isolated in Figure 14(d). Such peaks do not appear in the short-die case, see Figure 5(f), and hence are a new introduction as a consequence of the full-die and melt-wire contact.

Top surface shear stress profiles of Figure 17(a) demonstrate the “localised effects“ of die-exit point discontinuity for a range of meshes. Shear stress in the free-jet region reduces and reflects mesh convergence with refinement. A violent jump in solution is observed over the land region. Discrepancies between the various PTT model results for shear stress are illustrated in Figure 17(b). Performance of the quadratic PTT model is notably quite poor at the die-exit, with a sharp-decay in T_{rz} on the approach to the die-exit, followed by a leap to 0.4 units at the actual exit. Comparison of T_{rz} between full-die and short-die pressure-tooling instances reveals a 2.7 times increase in maximum value for the quadratic PTT, and 1.8 times increase for the exponential PTT version (Tables 4 and 7). *Such oscillations in T_{rz} are magnified greatly with the linear PTT model, rendering satisfactory convergence impossible*. This is a reflection of accessing these severe industrial-level dynamical ranges. Shear stresses along the bottom surface (Figure 18(a)) reveal the significant influence of the moving-wire on the flow at the melt-wire contact point (axial position –1.1 units, indicated by arrow in Figures 16-20), and the loss of accurate resolution on the coarse mesh in regions of high activity (sharp gradients). The “first impact” effect of the moving wire on the fluid at position –1.1 units is magnified in Figure 18(b). This is evidence to the effects of the drag flow. The shear stress profile for

the exponential PTT model is on the other hand, minimally affected with oscillation in this contact zone.

There is little difference in axial stress behaviour along the *top surface*, between the various levels of mesh refinement (Figure 19(a)). That is, with the exception of local adjustment around the sharp geometric corners of the die and within the extrudate. Notably, in the extrudate, T_{zz} remains positive on medium and fine meshes, providing some residual stress to the coating, albeit small. The axial stress of the quadratic PTT model (Figure 19(b)) is seen to peak at 0.65 units within the land region, some 4.3 times greater than that for short-die, pressure-tooling (compare with Tables 4 and 7). The exponential PTT model T_{zz}-profile increases only slightly, with T_{zz} for full-case pressure-tooling, reaching a magnitude 1.7 times larger than that for the short-die instance. Along the *bottom surface* in Figure 20(a), the finer mesh refinement is observed to give smoother transitions in axial stress. The characteristic "double peak" profile at the melt-wire contact point and die-exit regions is observed in the axial stress in Figure 20(b). Notably for the quadratic model, the axial stress peak at the melt-wire contact point exceeds that at die-exit and is followed by a sharp relaxation on the approach to the land region, upon which a more sustained maxima forms. Again, the exponential PTT model provides smoother damped results, much reduced in magnitude, than those for the quadratic case. Hence, along the wire, there is a ten-fold increase in values for the quadratic PTT model observed from short to full-die pressure-tooling (Figure 11(c) and 20(b)). For the exponential PTT model, correspondingly, there is little change.

Die-swell profiles along the top free surface (Figure 21(a)) increase progressively with mesh refinement. This demonstrates the need for serious care and attention to sufficient mesh refinement, if accurate die-swell predictions are required. The fine biased mesh provides such. Quadratic and exponential PTT die swell projections from the die-exit (Figure 21(b)) show little variation, due to the intensity of mesh refinement employed on the biased fine mesh. The swelling ratio corresponding to the exponential PTT model is 15% larger than that for short-die pressure-tooling. A similar observation holds likewise for the quadratic PTT model, there showing a 14% difference (Tables 4 and 7).

8. CONCLUSIONS

Overall, the short-die pressure-tooling study indicated solution variation with parameters μ_1 and *We*, and response of various PTT models. Ranges of shear and extension rate were of order 10^2 and 10^{-1}, respectively. The linear, quadratic and exponential PTT models were computed for the short-die, and demonstrate the influence of shear and extensional viscosity variations. For short-die flow, there was no melt-wire sudden contact and smooth solutions were established on the wire at the die-exit. For the full-die study, equivalent solution trends are established with parameter adjustment in μ_1 and *We*. Stable solutions were only available for the strain-softening models of quadratic and exponential PTT form. Ranges of shear and extension rate rose above the short-die case to orders 10^3 and 10^1, respectively. For dimensional equivalents, one must scale by $O(10^3)$.

For the *short-die tooling*, the major observations are summarised as follows. Maximum shear rates arise at die-exit, top-surface, whilst for extension rates they lie within the free-jet region. Such maxima in shear rate are suppressed with increasing *We*, but increase with increase of μ_1. The corresponding situation for strain rates is more marked, but displaying similar trends to shear rate. Also, increasing μ_1 is seen to magnify

die-swell. With adjustment of model, (linear, quadratic to exponential) maxima in shear rates increase, whilst they consistently fall for strain rates. Smooth solution profiles result for quadratic/exponential PTT, in contrast to those for the linear PTT. This distinguishes the influence of strain-hardening from softening and its effect upon numerical stability. Strain-hardening effects are responsible for the oscillations (around die-exit) with the linear PTT model top-surface profiles in variables I_2, T_{rz} and T_{zz}. Shear-thinning and strain-softening stabilise the position for quadratic and exponential PTT model variants, rendering stable numerical solutions. Due to shear-thinning at the larger *We*-values, stress levels almost vanish. Axial stress maxima at top surface are due to mild strain-softening. Along the wire, axial stress peaks occur beyond the die for linear PTT, just within the die for quadratic PTT and practically vanish for exponential PTT. Similar comments apply for shear stress.

For the *full-die tooling*, solution oscillations, mainly around the die-exit singularity, are greatly magnified with the linear PTT model and prevent convergence at industrial-level deformation rates. Shear rate maxima on the top surface occur over the land-region, and in particular, peak at the die-exit. The level is some fifteen times larger than that for the short-die. Shear rate maxima on the wire are lower than that at the top surface, by a factor of three. The double (sudden shock) peaks in shear rates at the bottom surface for full-die flow, do not appear in the short-die case. These are a new feature, introduced as a consequence of the full-die and melt-wire contact. There is a double peak along the wire, with the die-exit value being marginally larger than that at melt-wire contact. Extension rate maxima are lower than shear rates by one order, but have increased one hundred fold from the short-die case. Extension rates peak at the melt-wire contact and across land/die-exit region. The maximum corresponds to the die-exit. The pressure drop across the flow is almost entirely confined to the land-region, and is magnified some twenty two times over that for the short-die.

The behaviour in stress for full-tooling reveals the "shock impact" as the fluid makes contact with the wire is most prominent in the stress. The largest axial stress arises within the free jet-entry region. For the quadratic PTT model, stress along the bottom surface is greatly influenced by the drag flow effects imposed on the fluid by the moving wire. For the exponential PTT model, the corresponding stress behaviour, is on the other hand, only marginally affected by oscillations in this contact zone. Greater mesh refinement is seen to give smoother transitions of axial stress along the bottom surface. For the quadratic PTT model, the axial stress peak at the melt-wire contact point exceeds that at die-exit, and is followed by a sharp relaxation on the approach to the land region. Thereupon, a more sustained maxima forms giving, the characteristic "double peak" profiles. The exponential PTT model is again seen to provide smoother, more damped, axial stress variations than occur for the quadratic case. Die-swell profiles along the top free surface increase progressively with mesh refinement, demonstrating mesh convergence. The swelling ratios for the quadratic and exponential PTT models are 15% higher than that observed for short-die tooling. Hence, the influence of the die flow itself is exposed.

FIGURE LEGEND

References

1. H. Matallah and P. Townsend and M. F. Webster, ‘Viscoelastic Multi-Mode Simulations of Wire-Coating’, J. Non-Newtonian Fluid Mech., vol 90, pp 217-241, (2000)
2. D. M. Binding and A. R. Blythe and S. Gunter and A. A. Mosquera and P. Townsend and M. F. Webster, ‘Modelling Polymer Melt Flows in Wire Coating Processes’, J. Non-Newtonian Fluid Mech., vol 64, pp 191-209, (1996).
3. S. Gunter and P. Townsend and M. F. Webster, ‘The Simulation of Some Model Viscoelastic Extensional Flows’, Int. J. Num. Meth. Fluids, vol 23, pp 691-710, (1996).
4. I. Mutlu and P. Townsend and M. F. Webster, ‘Simulation of Cable-Coating Viscoelastic Flows with Coupled and Decoupled Schemes’, J. Non-Newtonian Fluid Mech., vol 74, pp 1-23, (1998).
5. I. Mutlu and P. Townsend and M. F. Webster, ‘Computation of Viscoelastic Cable Coating Flows’, Int. J. Num. Meth. Fluids, vol 26, pp 697-712, (1998).
6. F. P. T. Baaijens, S. H. A. Selen, H. P. W. Baaijens, G. W. M. Peters and H. E. H. Meijer, ‘Viscoelastic Flow Past a Confined Cylinder of a LDPE Melt’, J. Non-Newtonian Fluid Mech., vol 68, pp 173-203, (1997).
7. H. P. W. Baaijens, ‘Evaluation of Constitutive Equation for Polymer Melts and Solutions in Complex Flows’, Thesis, Eindhoven University of Technology, Netherlands, 1994.
8. V. Ngamaramvaranggul and M. F. Webster, ‘Simulation of Coating Flows with Slip Effects’, Int. J. Num. Meth. Fluids, in press 2000.
9. V. Ngamaramvaranggul and M. F. Webster, ‘Computation of Free Surface Flows with a Taylor-Galerkin/Pressure-Correction Algorithm’, Int. J. Num. Meth. Fluids, in press 2000.
10. V. Ngamaramvaranggul and M. F. Webster, ‘Viscoelastic Simulations of Stick-Slip and Die-Swell Flows’, Int. J. Num. Meth. Fluids, under review 2000, available as CSR 15-2000, University of Wales, Swansea.
11. Z. Tadmor, R. B. Bird, ‘Rheological Analysis of Stabilizing Forces in Wire-Coating Die’, Polym. Eng. Sci., vol 14, no. 2, pp 124-136, (1974).
12. B. Caswell and R. I. Tanner, ‘Wire Coating Die Design Using Finite Element Methods’, J. Polym. Sci., vol 18, no. 5, pp 416-421, (1978).
13. J. F. T. Pittman and K. Rashid, ‘Numerical Analysis of High-Speed Wire Coating’ Plast. Rub. Proc. Appl., vol 6, p 153, (1986).
14. E. Mitsoulis, ‘Finite Element Analysis of Wire Coating’, Polym. Eng. Sci., vol 26, no. 2, pp 171-186, (1986).
15. E. Mitsoulis and R. Wagner and F. L. Heng, ‘Numerical Simulation of Wire-Coating Low-Density Polyethylene: Theory and Experiments’, Polym. Eng. Sci., vol 28, no. 5, pp 291-310, (1988).
16. R. Wagner and E. Mitsoulis, Adv. Polym. Techno., vol 5, p 305 (1985).
17. E. Mitsoulis, J. Vlachopoulos and F. A. Mirza, ‘Numerical Simulation of Entry and Exit Flows in Slit Dies’, Polym. Eng. Sci., vol 24, no.9, pp 707-715, (1984).

18. B. Arpin, P. G. Lafleur and V. Lenir, ‘Computer Aided Design of Wire Coating Dies’, ANTEC 91, pp 58-61, (1991).

19. C. D. Han and D. Rao, ‘Studies on Wire Coating Extrusion. I. The Rheology of Wire Coating Extrusion’, Polym. Eng. Sci., vol 18, no.13, pp 1019-1029, (1978).

20. E. Mitsoulis, ‘Fluid Flow and Heat Transfer in Wire Coating: a review’, Adv. polym. Technol., vol 6, no. 4, pp 467-487, (1986).

21. J. F. Carley, T. Endo and W. B. Krantz, ‘Realistic Analysis of Flow in Wire-Coating Die’, Polym. Eng. Sci., vol 19, no. 16, pp 1178-1187, (1979).

22. T.- S. Chung, ‘The Effect of Melt Compressibility on a High-Speed Wire-Coating Process’, Polym. Eng. Sci., vol 26, no. 6, pp 410-414, (1986).

23. K. U. Haas and F. H. Skewis, SPE ANTEC Tech. Paper, vol 20, p 8, 1974.

24. H. Matallah and P. Townsend and M. F. Webster, ‘Viscoelastic Computations of Polymeric Wire-Coating Flows’, Int. J. Num. Meth. Eng., under review 2000, available as CSR 13-2000, University of Wales, Swansea.

25. N. Phan-Thien and R. I. Tanner, ‘A New Constitutive Equation Derived from Network Theory’, J. Non-Newtonian Fluid Mech., vol 2, pp 353-365, (1977).

26. N. Phan-Thien, ‘A Non-linear Network Viscoelastic Model’, J. Rheol., vol 22, pp 259-283, (1978).

27. R. B. Bird, R. C. Armstrong and O. Hassager, ‘Dynamics of Polymeric Liquids’, Fluid Mechanics, vol 1, 2nd Edn., Wiley, New York, 1987.

28. E. O. A. Carew and P. Townsend and M. F. Webster, ‘A Taylor-Petrov-Galerkin Algorithm for Viscoelastic Flow’, J. Non-Newtonian Fluid Mech., vol 50 , pp253-287, (1993).

29. M. J. Crochet, A. R. Davies and K. Walter,’Numerical Simulation of Non-Newtonian Flow’, Rheology Series 1, Elsevier Science Publishers, 1984.

30. N. Phan-Thien and R. I. Tanner, ‘Boundary-Element Analysis of Forming Processes' in 'Numerical Modelling of Material Deformation Processes: Research, Development and Application’ by P. Hartley, I. Pillinger and C. Sturgess (Eds) Springer-Verlag, London, 1992.

31. V. Ngamaramvaranggul and M. F. Webster, ’DSM Contract Continuous Coating of Glass Rovings’, Private Communication for DSM Research, Nov/Dec 1997.

32. R. B. Bird and M. W. Johnson and J. F. Stevenson, Paper Presented at the Int. Congr. Rheol., 5th Kyoto, Japan October, 1968.

33. G. Marrucci and G. Titomanlo and G. C. Sarti, ‘Testing of a Constitutive Equation for Entangled Networks by Elongational and Shear Data of Polymer Melt’, Rheol. Acta, vol 12, pp 269-275, (1973).

34. R. I. Tanner, ‘Comparative Studies of Some Simple Viscoelastic Theories’, Trans. Soc. Rheol., vol 12, pp 155-182, (1968).

35. C. D. Han and J. Y. Park, J. Appl. Polym. Sci., vol 19, p 3257, (1975).

36. N. E. Hudson and J. Ferguson and P. Mackie, ‘The Measurement of Elongational Viscosity of Polymer Solutions Using a Viscometry of Novel Design’, vol 18, pp 541-562, (1974).

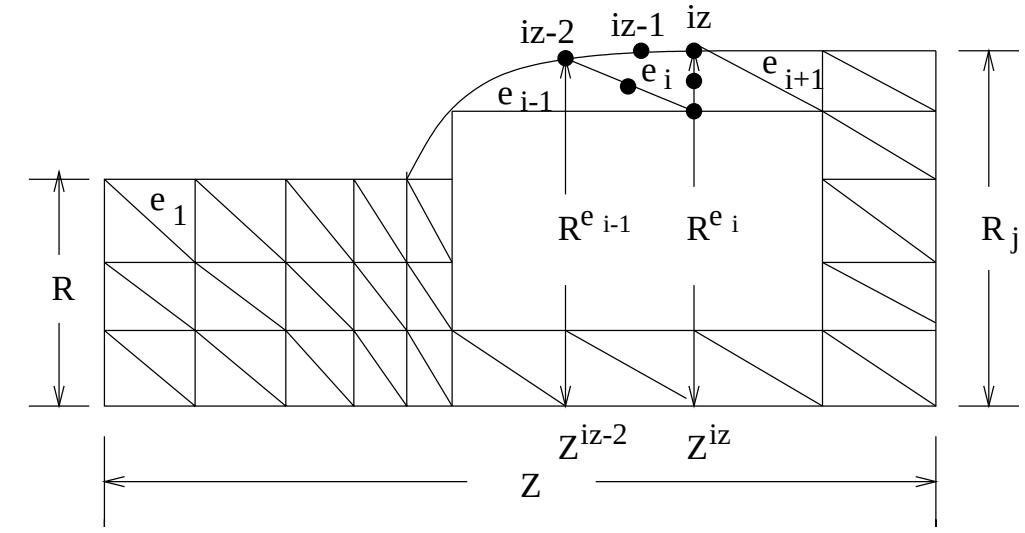

(a) **node-element referencing**

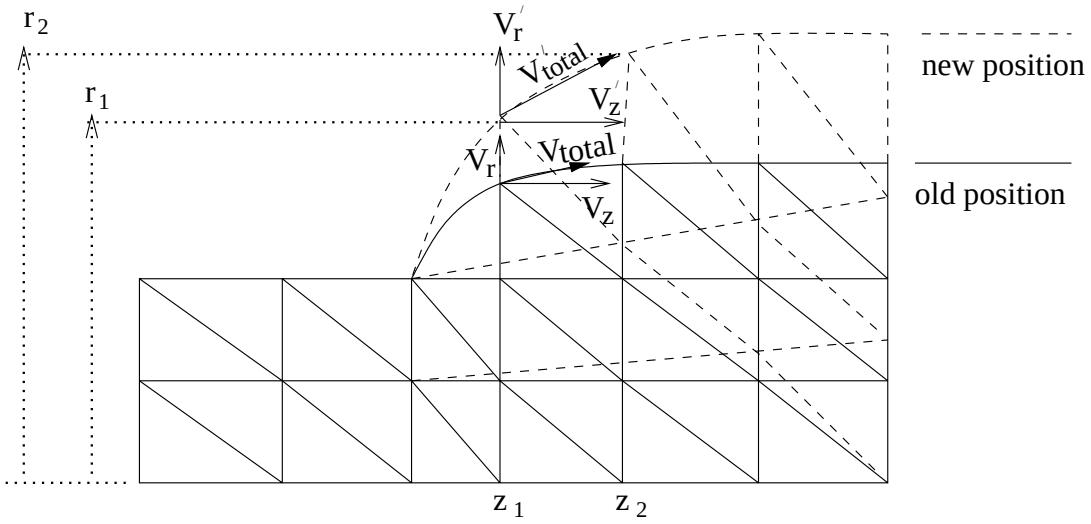

(b) **free surface adjustment**

Figure 1: **Extrudate region**

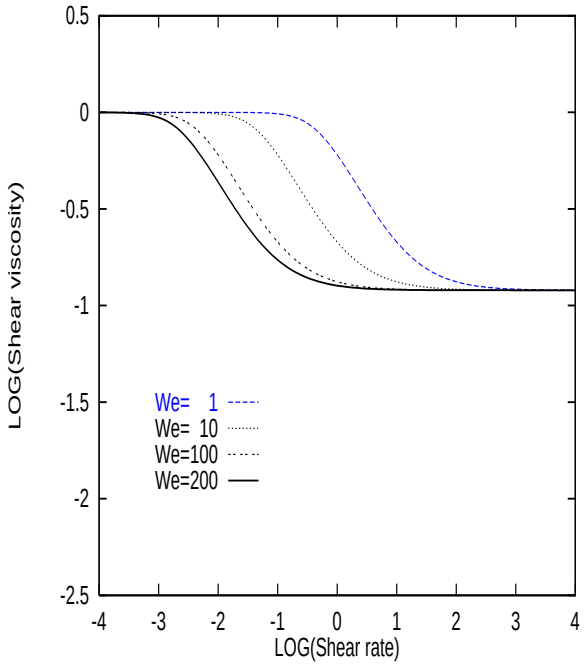

(a) **Exp PTT(1,0,0.88)**

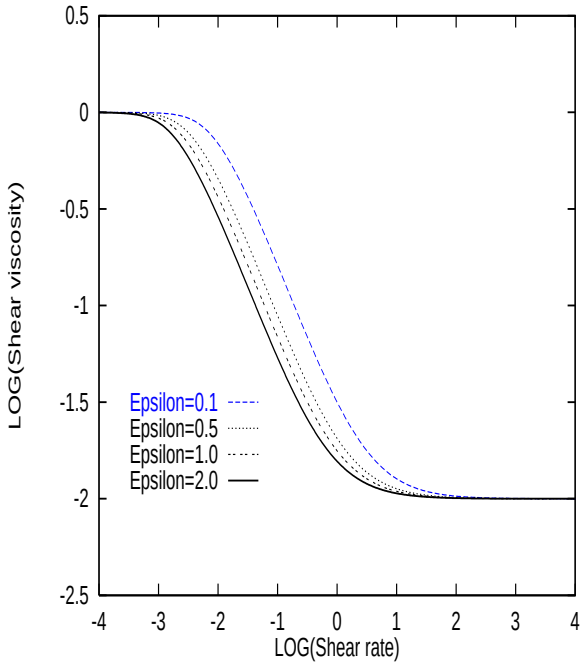

(b) **Exp PTT, μ_1=0.99, ξ=0, We=200**

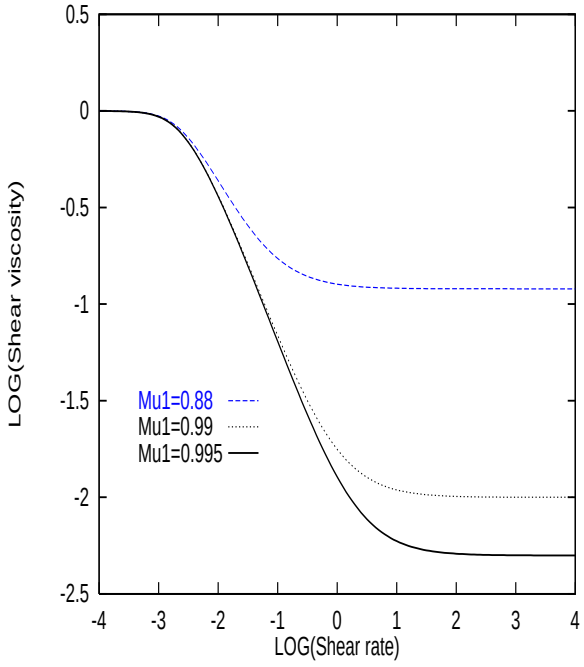

(c) **Exp PTT, ϵ=1, ξ=0, We=200**

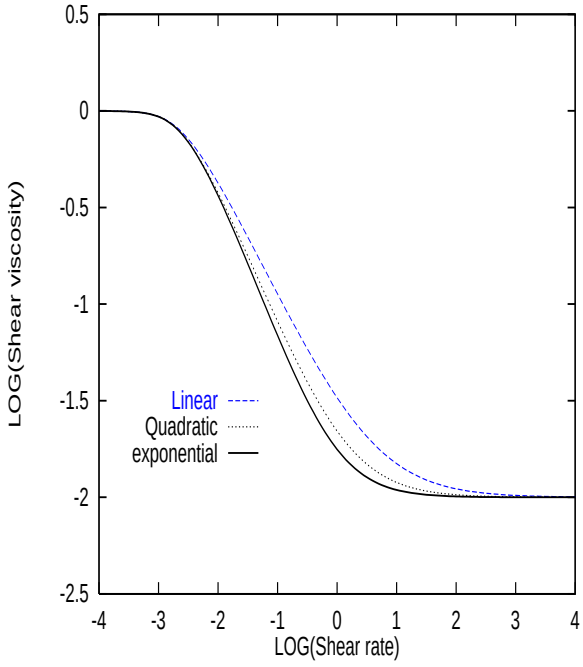

(d) **PTT(1,0,0.99), We=200**

Figure 2: **PTT model: shear viscosity**

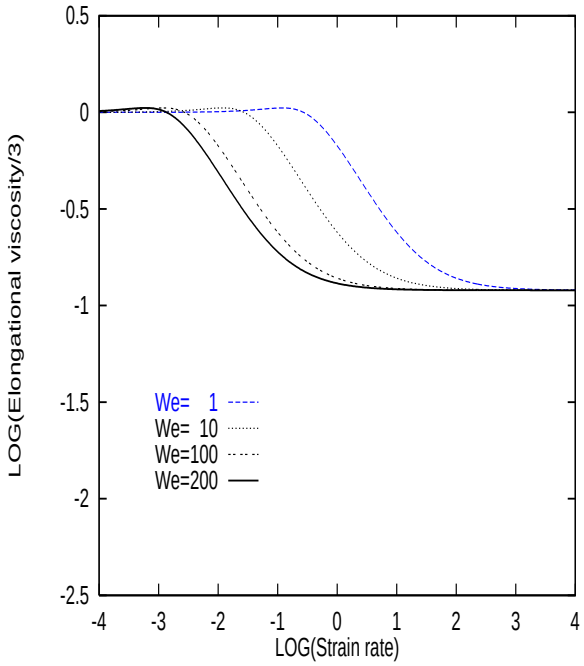

(a) **Exp PTT(1,0,0.88)**

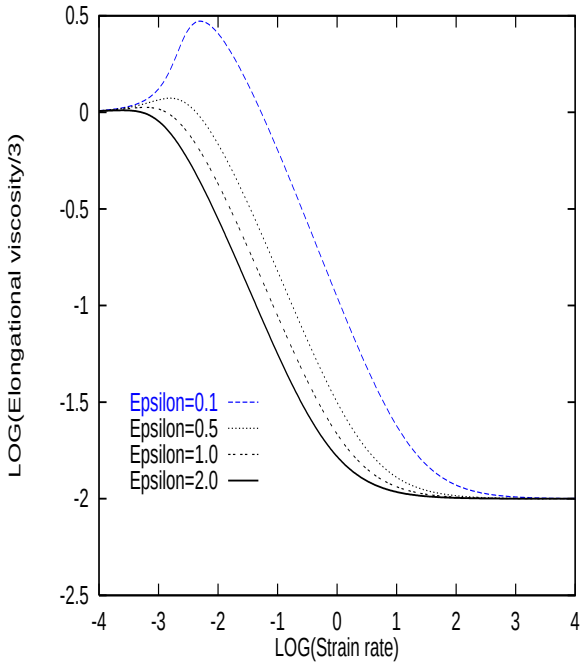

(b) **Exp PTT, μ_1=0.99, ξ=0, We=200**

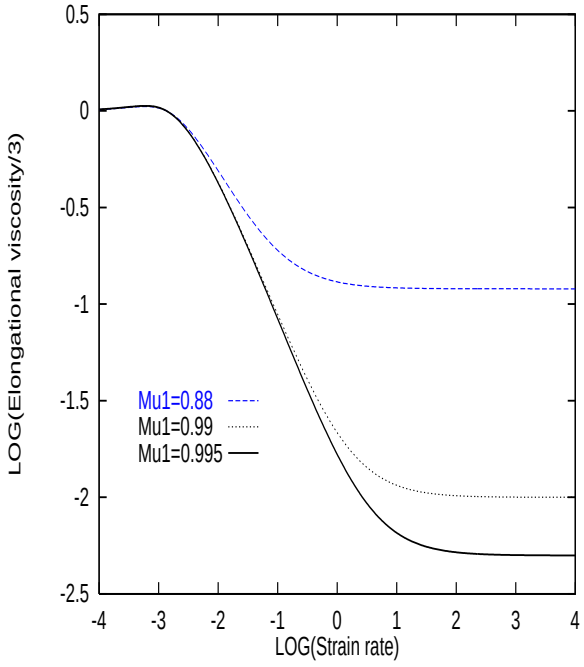

(c) **Exp PTT, ϵ=1, ξ=0, We=200**

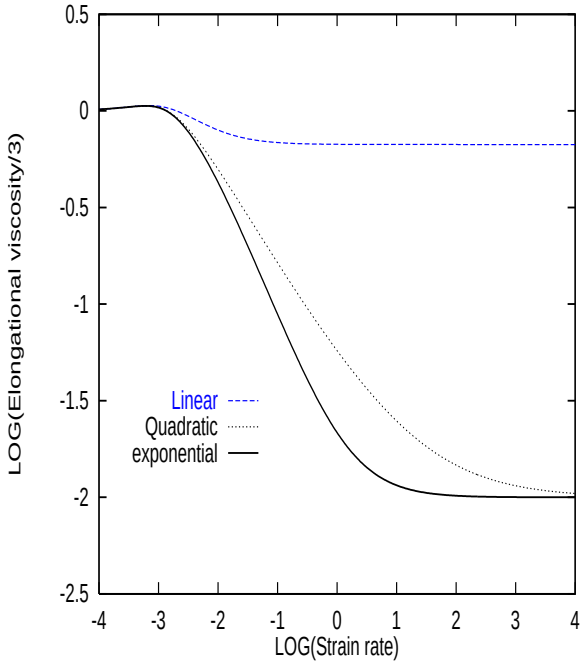

(d) **PTT(1,0,0.99), We=200**

Figure 3: **PTT model: elongational viscosity**

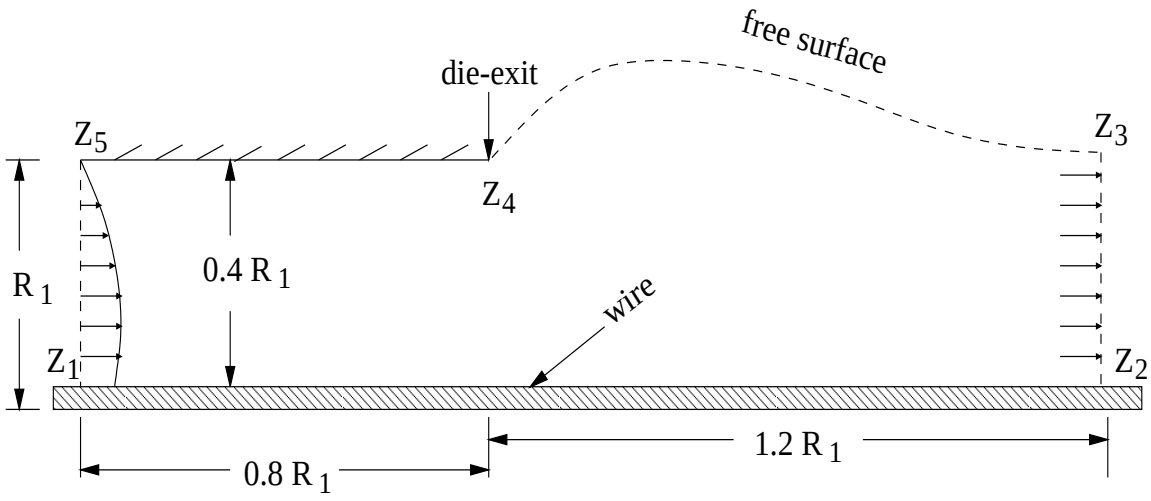

(a) **short-die pressure-tooling**

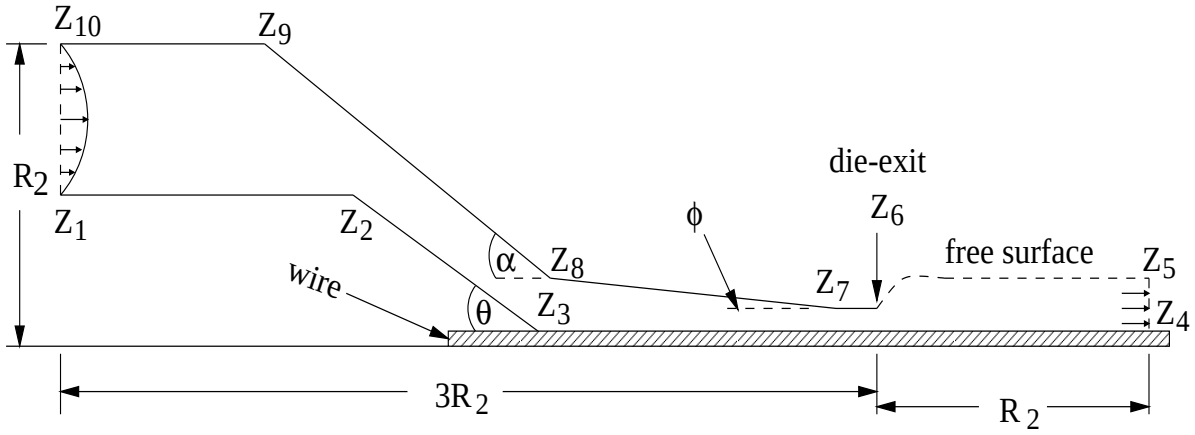

(b) **full-die pressure-tooling**

Figure 4: **Schema for extrusion coating flows**

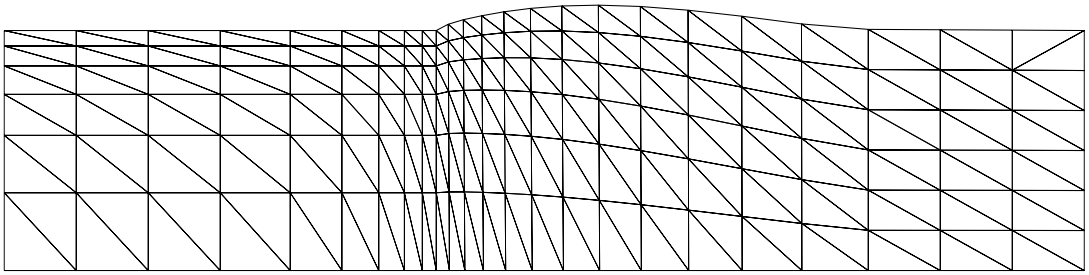

(a) **mesh pattern, 288 elements, 637 nodes**

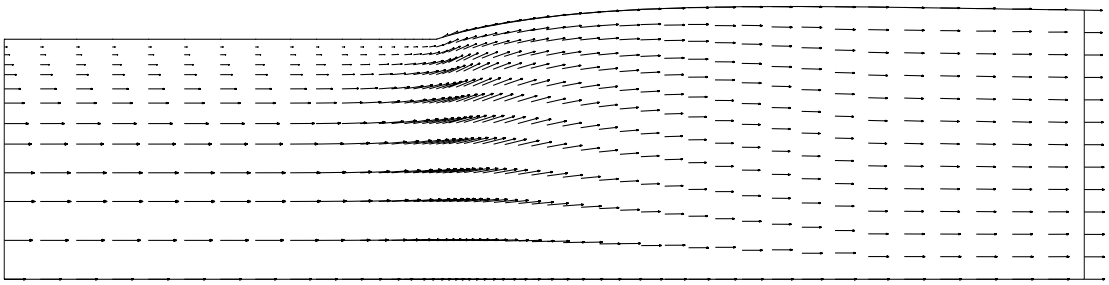

(b) **velocity vectors**

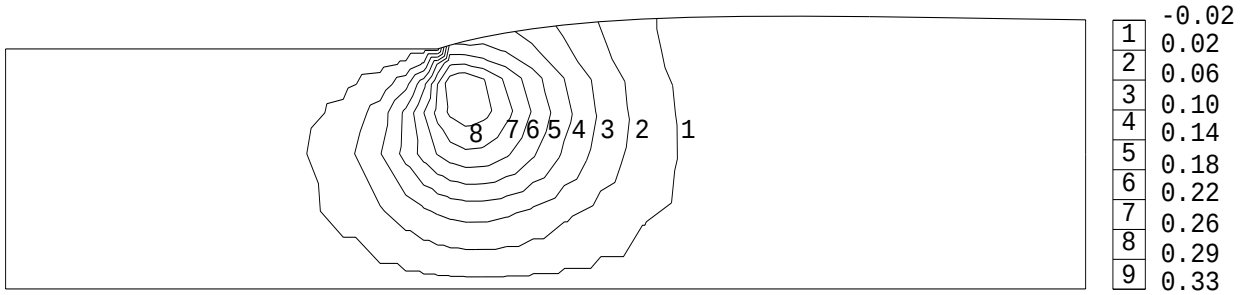

(c) V_r **contours**

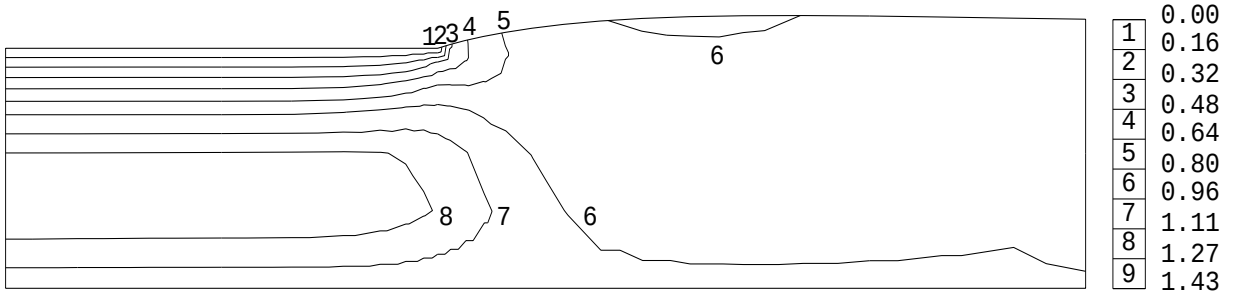

(d) V_z **contours**

Figure 5: **Short-die: exponential PTT(1,0,0.99)**, We**=200**

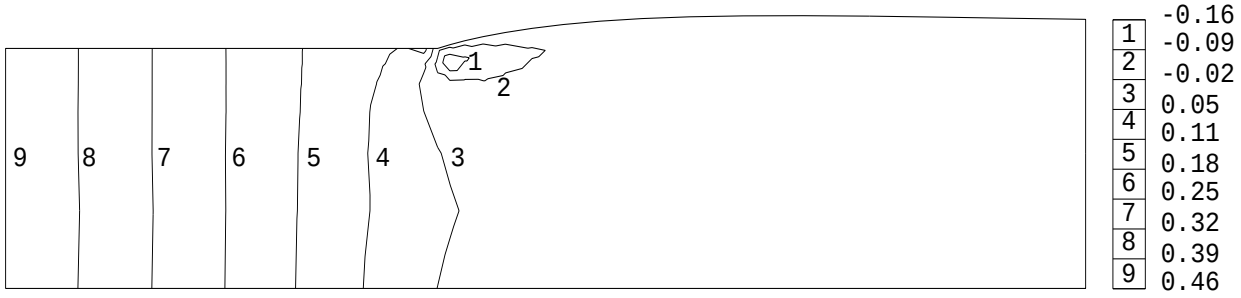

(e) **pressure contours**

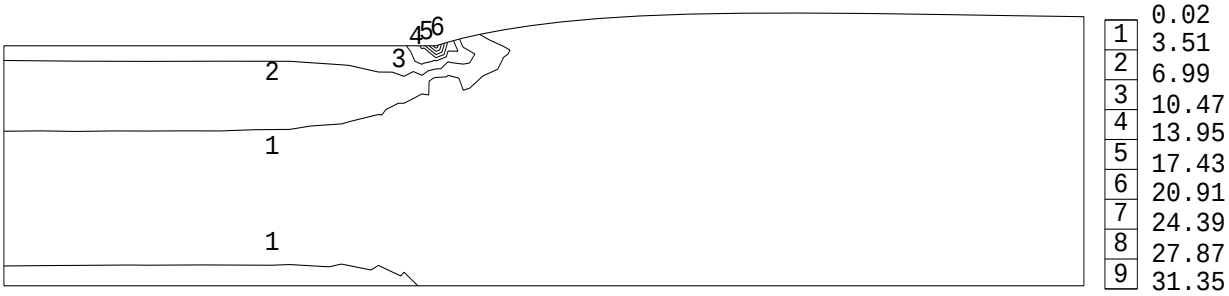

(f) I_2 **contours**

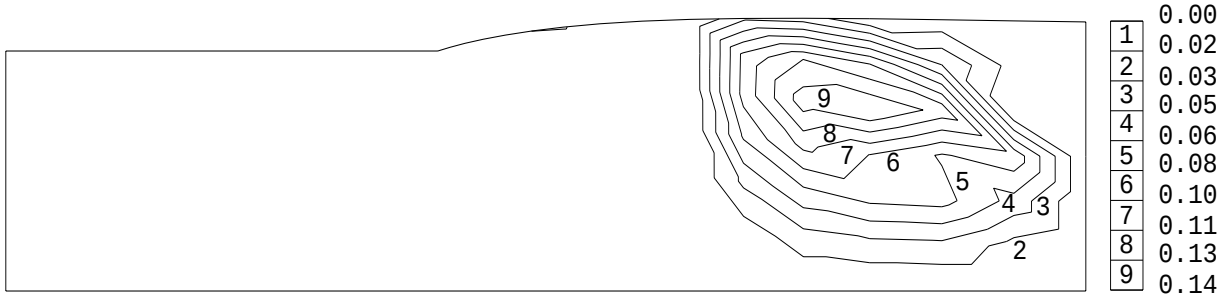

(g) $\dot{\epsilon}$ **contours**

Figure 5: Continued **Short-die: exponential PTT(1,0,0.99)**, We**=200**

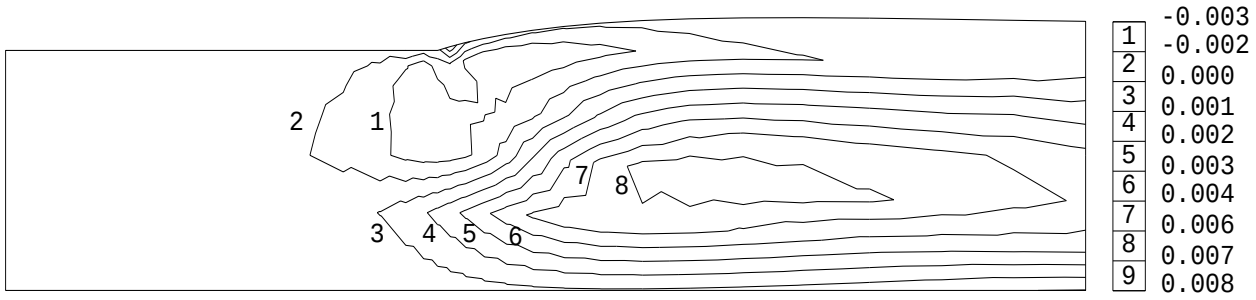

(h) T_{rr} **contours**

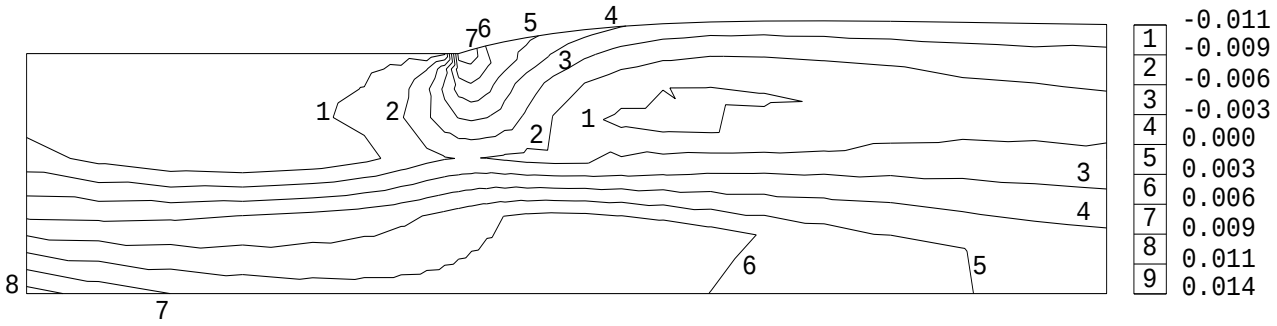

(i) T_{rz} **contours**

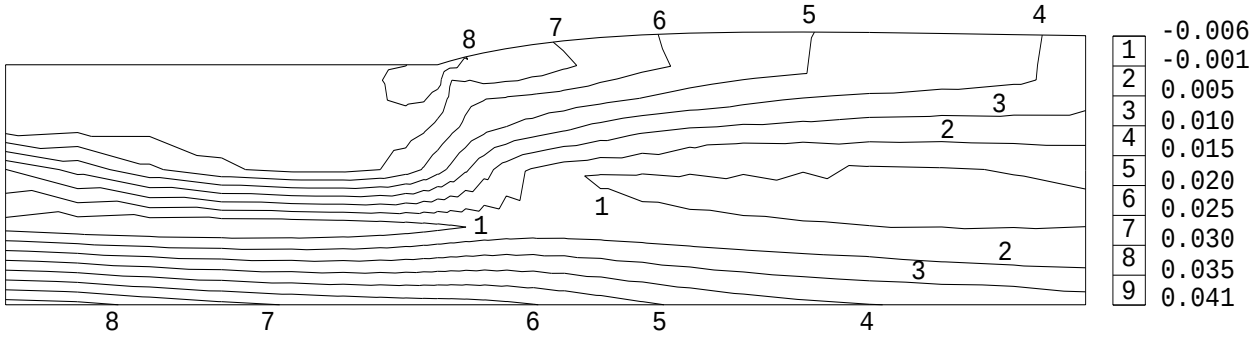

(j) T_{zz} **contours**

Figure 5: Continued **Short-die: exponential PTT(1,0,0.99)**, We**=200**

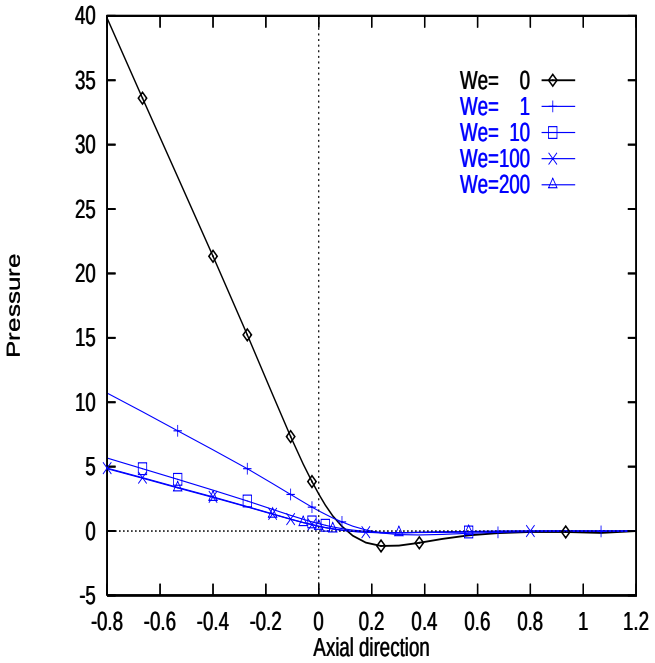

(a) **Exp PTT(1,0,0.88)**

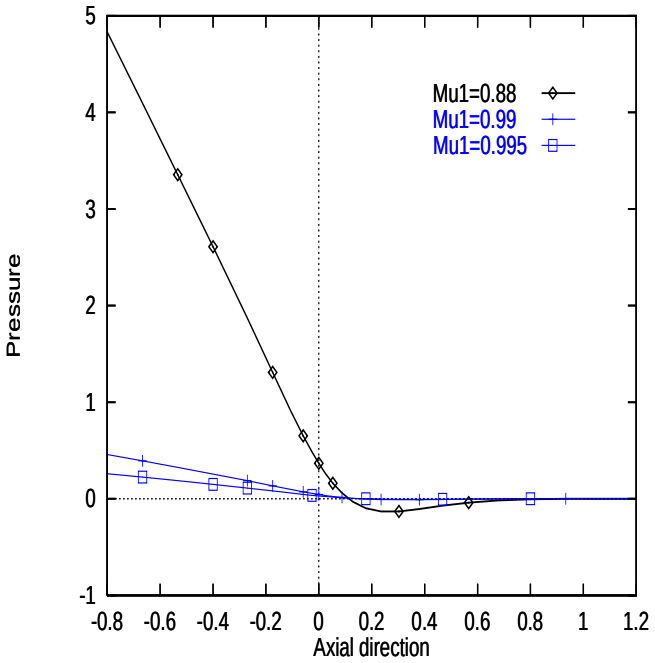

(b) **Exp PTT(1,0,μ_1), We=200**

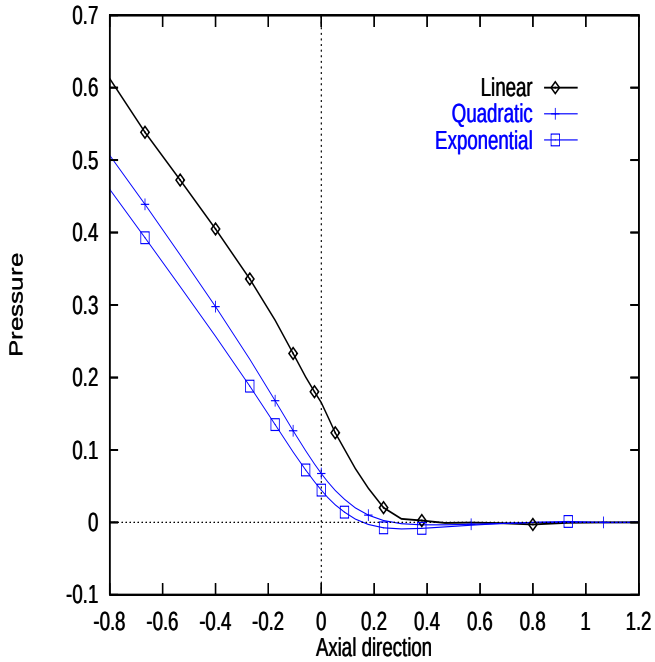

(c) **PTT(1,0,0.99), We=200**

Figure 6: **Short-die: PTT model, pressure along the wire; variation with (a) We, (b) μ_1, (c) model**

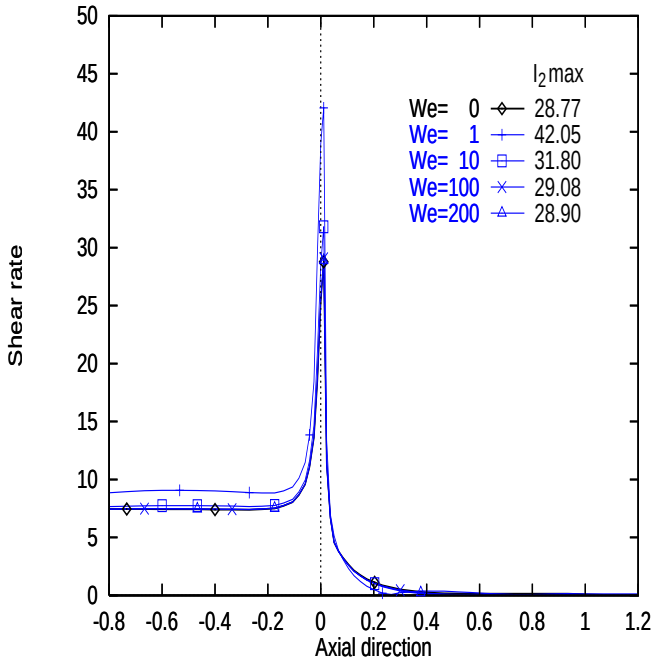

(a) **Exp PTT(1,0,0.88)**

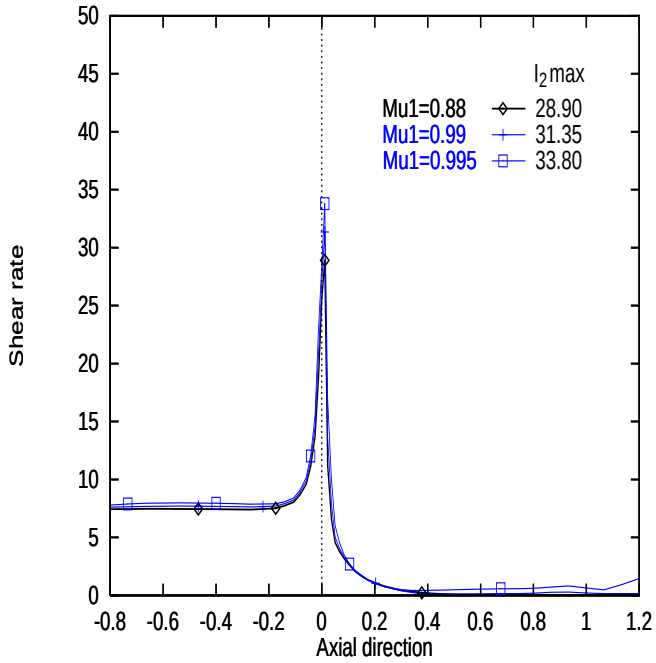

(b) **Exp PTT(1,0,μ_1), We=200**

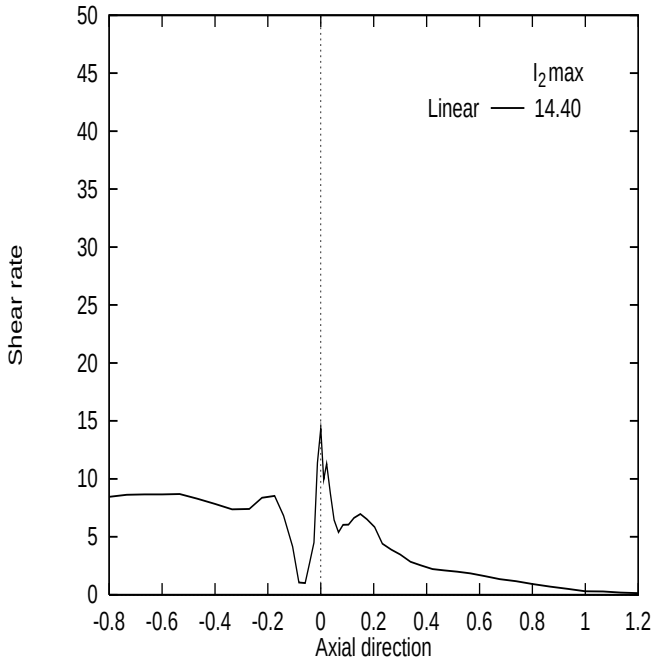

(c) **PTT(1,0,0.99), We=200**

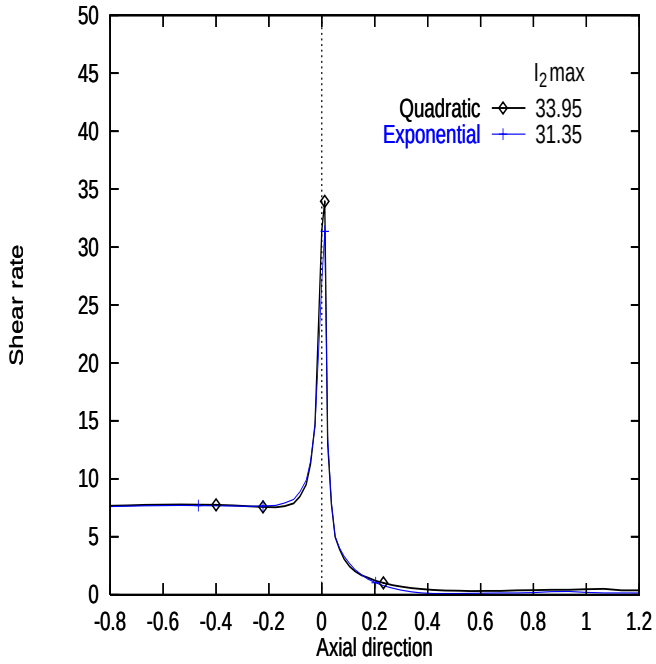

(d) **PTT(1,0,0.99), We=200**

Figure 7: **Short-die: PTT model, I_2 on top surface; variation with (a) We, (b) μ_1, (c) linear model, (d) model**

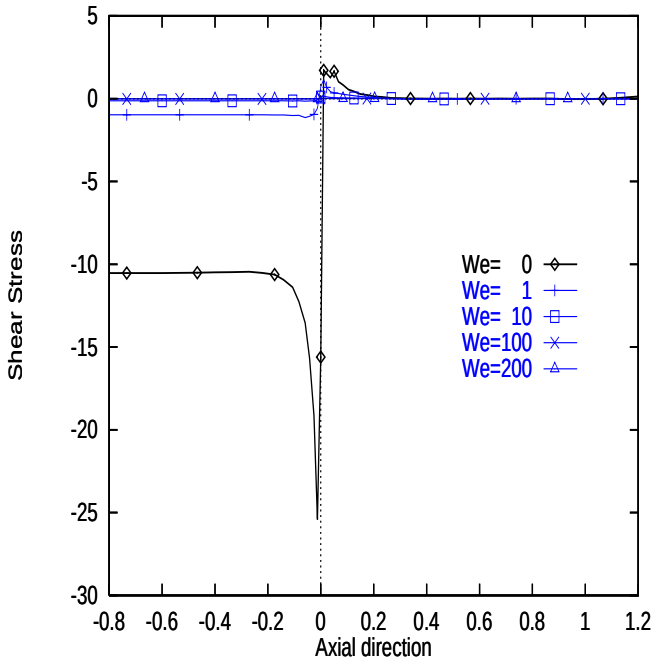

(a) **Exp PTT(1,0,0.88)**

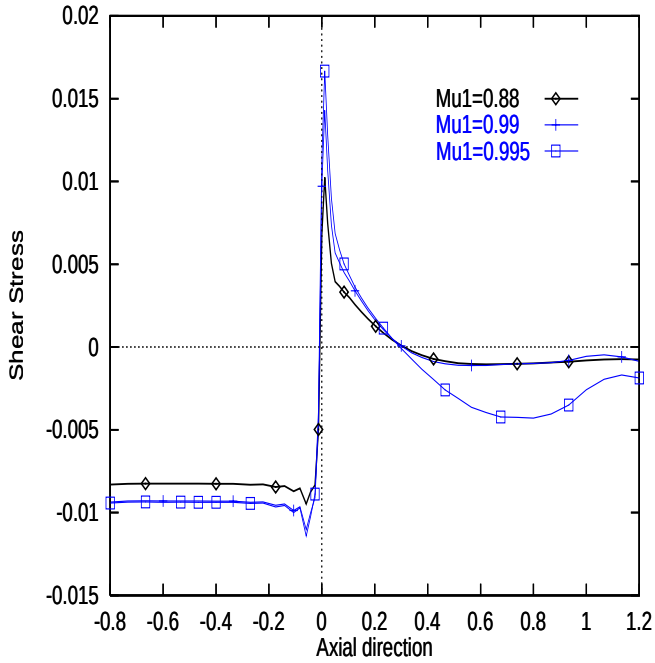

(b) **Exp PTT(1,0,μ_1), We=200**

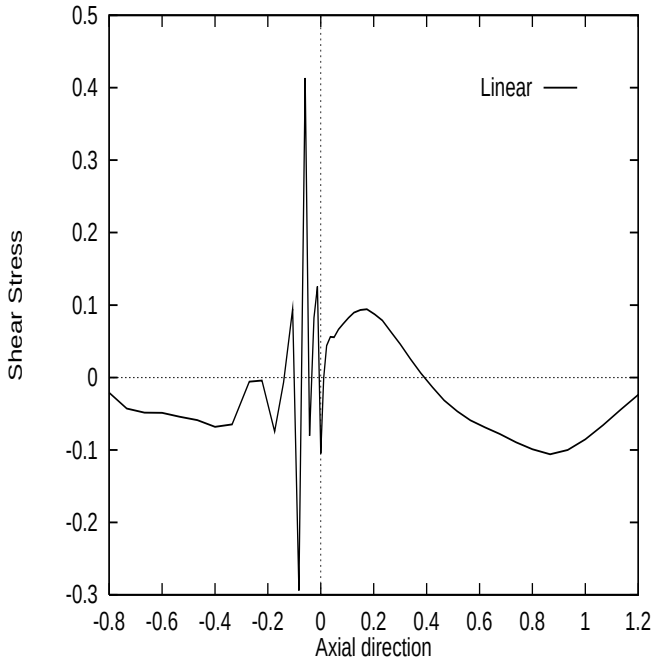

(c) **PTT(1,0,0.99), We=200**

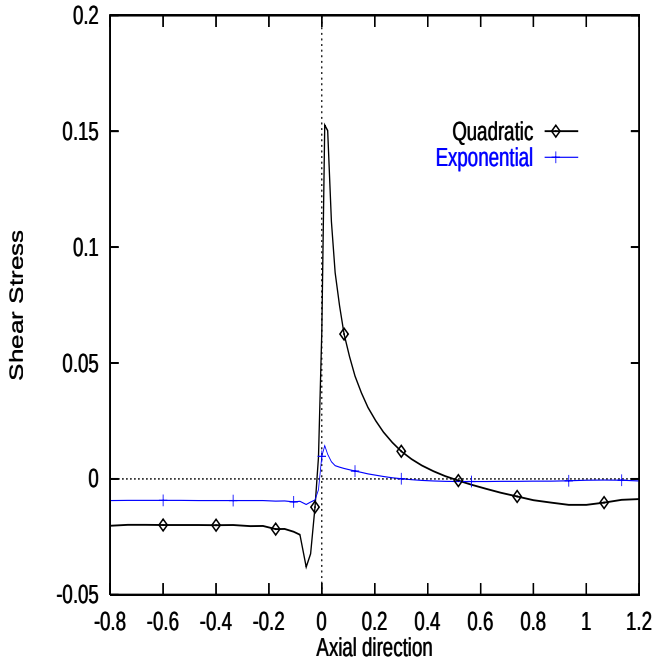

(d) **PTT(1,0,0.99), We=200**

Figure 8: **Short-die: PTT model, T_{rz} on top surface; variation with (a) We, (b) μ_1, (c) linear model, (d) model**

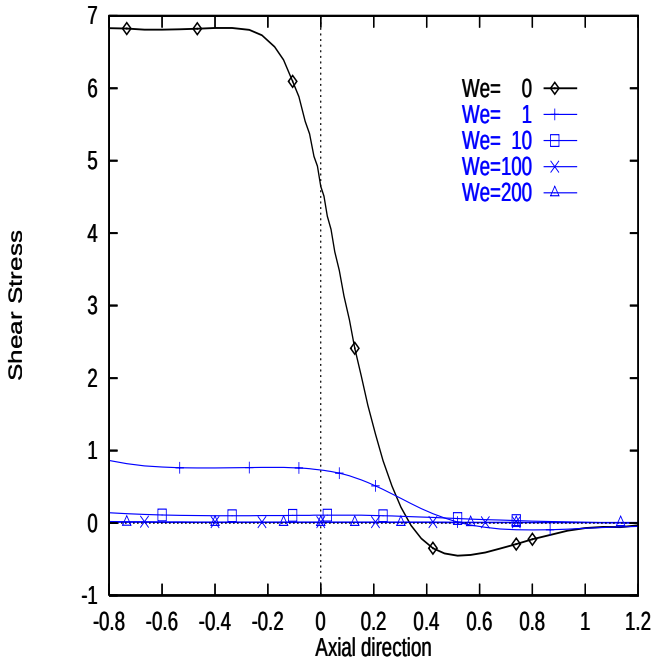

(a) **Exp PTT(1,0,0.88)**

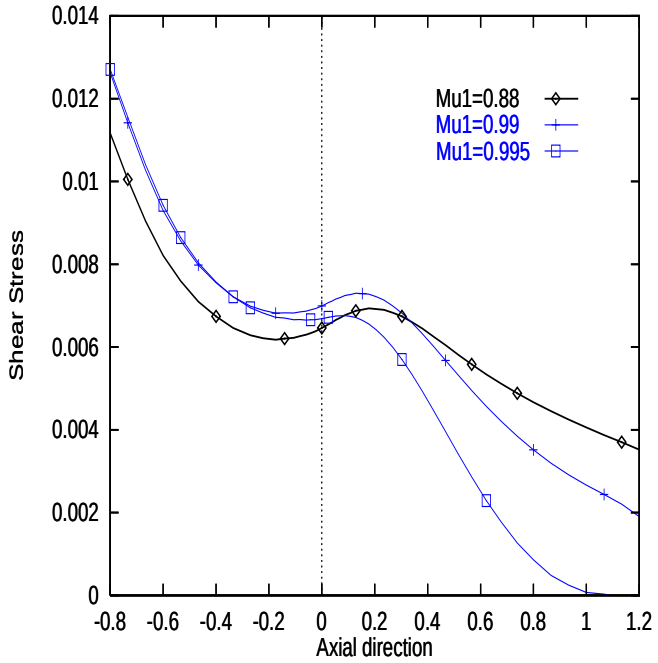

(b) **Exp PTT(1,0,μ_1), We=200**

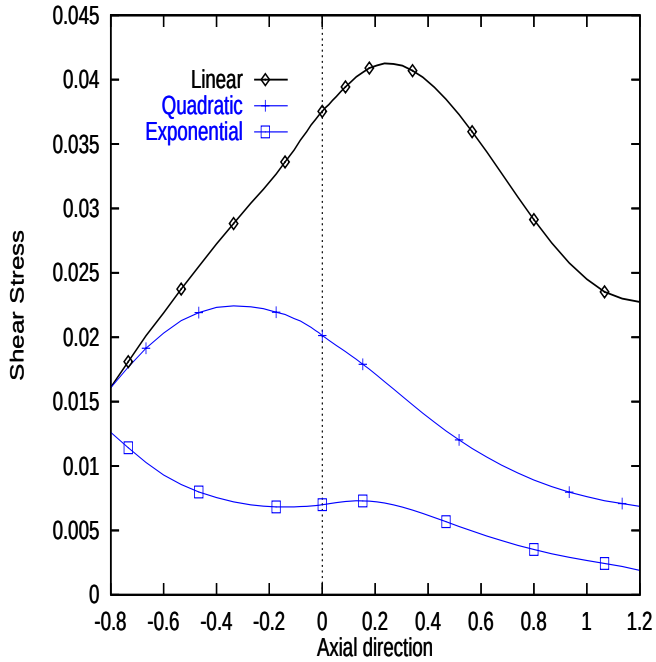

(c) **PTT(1,0,0.99), We=200**

Figure 9: **Short-die: PTT model, T_{rz} along the wire; variation with (a) We, (b) μ_1, (c) model**

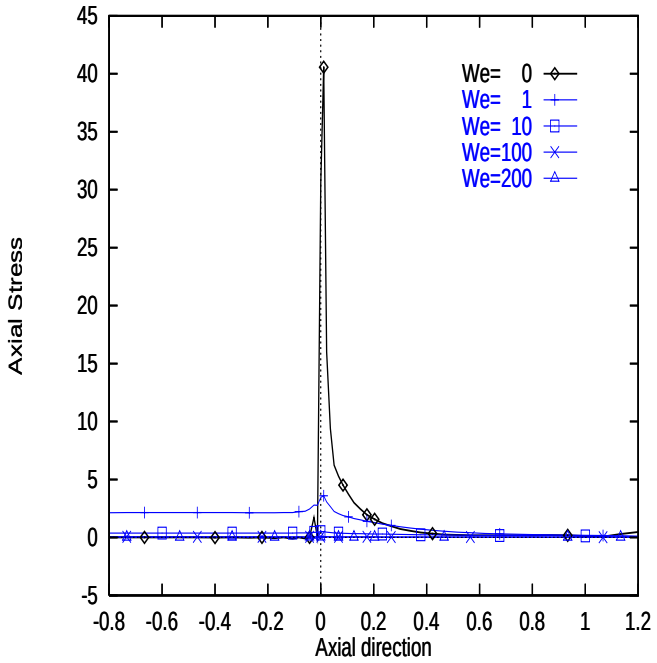

(a) **Exp PTT(1,0,0.88)**

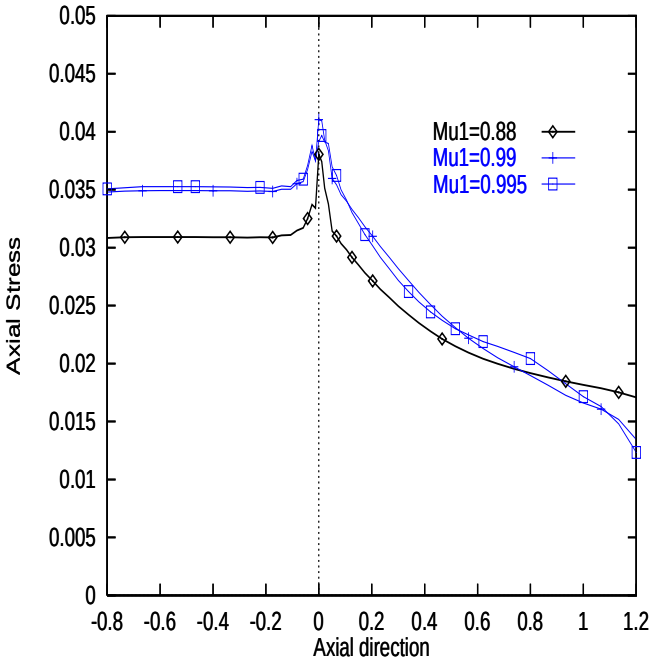

(b) **Exp PTT(1,0,μ_1), We=200**

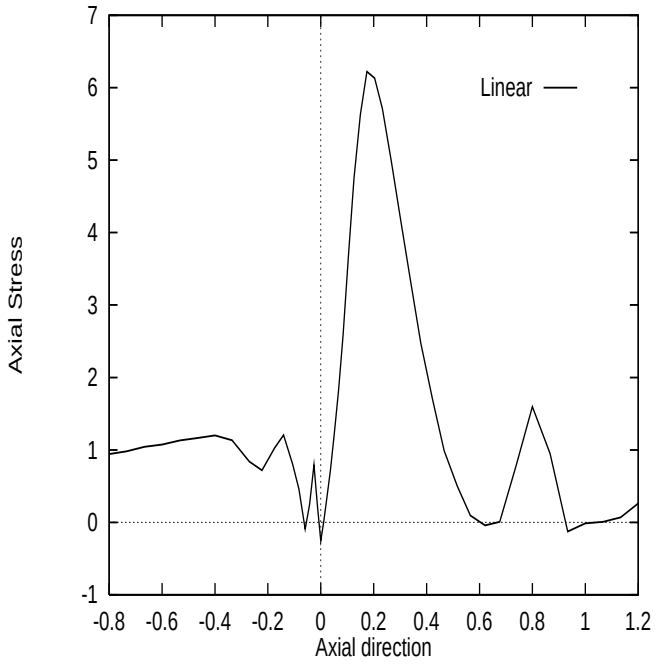

(c) **PTT(1,0,0.99), We=200**

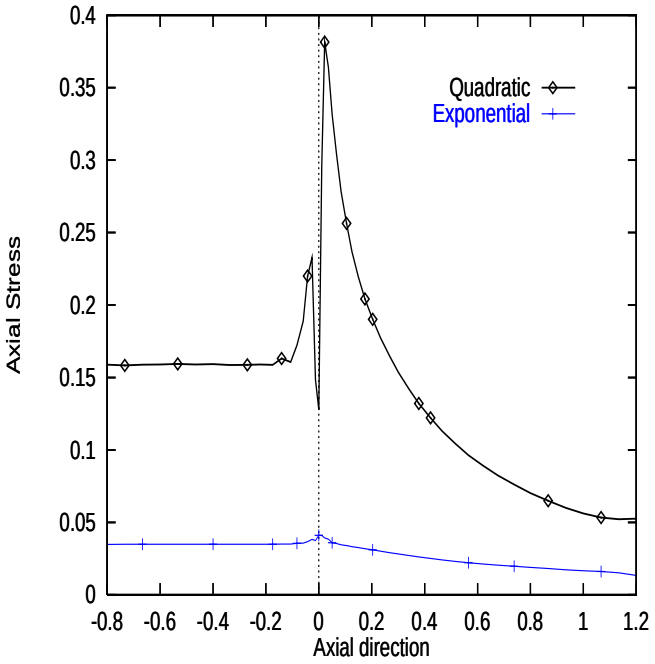

(d) **PTT(1,0,0.99), We=200**

Figure 10: **Short-die: PTT model, T_{zz} on top surface; variation with (a) We, (b) μ_1, (c) linear model, (d) model**

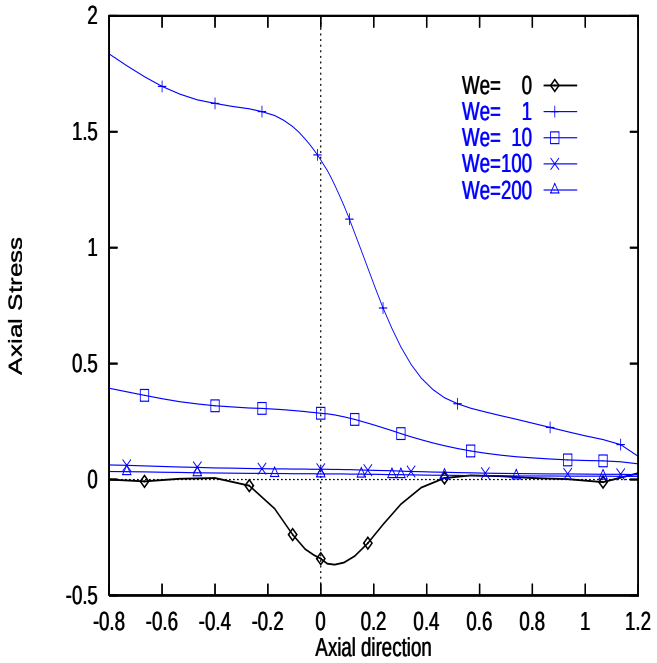

(a) **Exp PTT(1,0,0.88)**

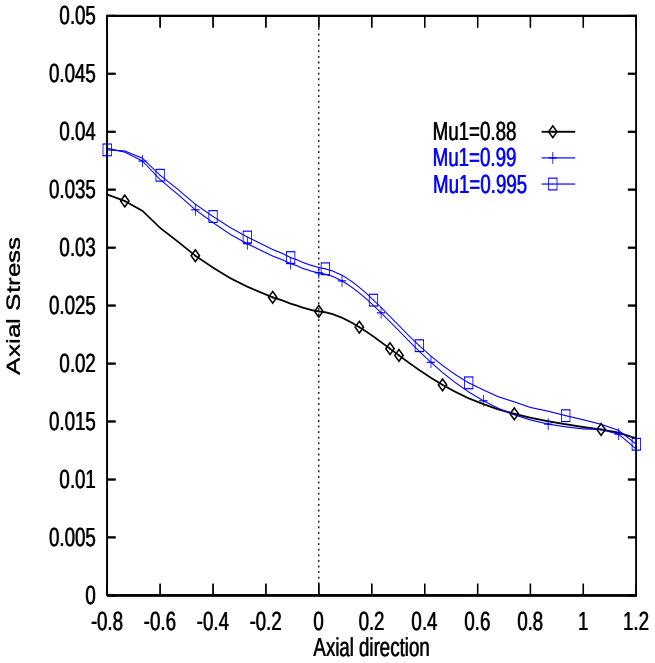

(b) **Exp PTT(1,0,μ_1), We=200**

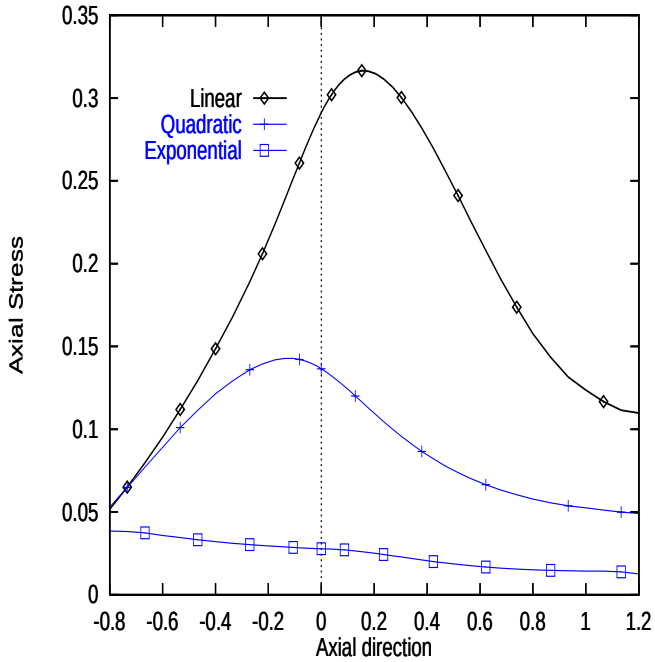

(c) **PTT(1,0,0.99), We=200**

Figure 11: **Short-die: PTT model, T_{zz} along the wire; variation with (a) We, (b) μ_1, (c) model**

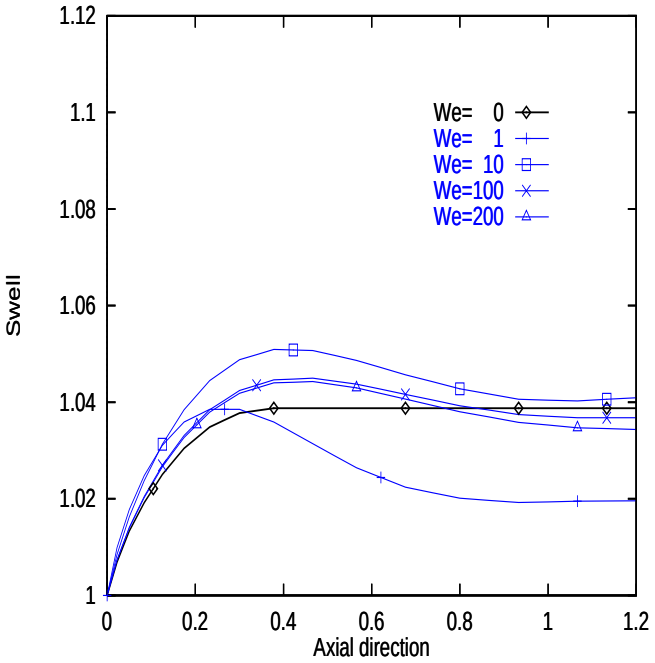

(a) **Exp PTT(1,0,0.88)**

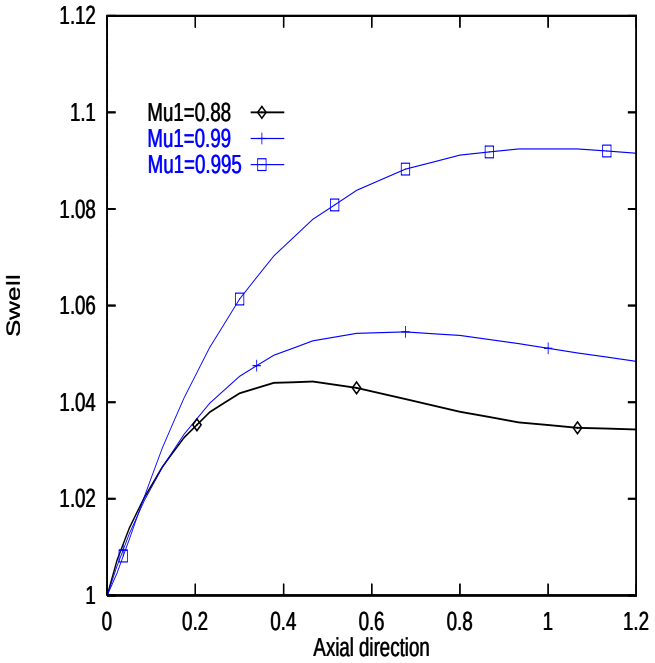

(b) **Exp PTT(1,0,μ_1), We=200**

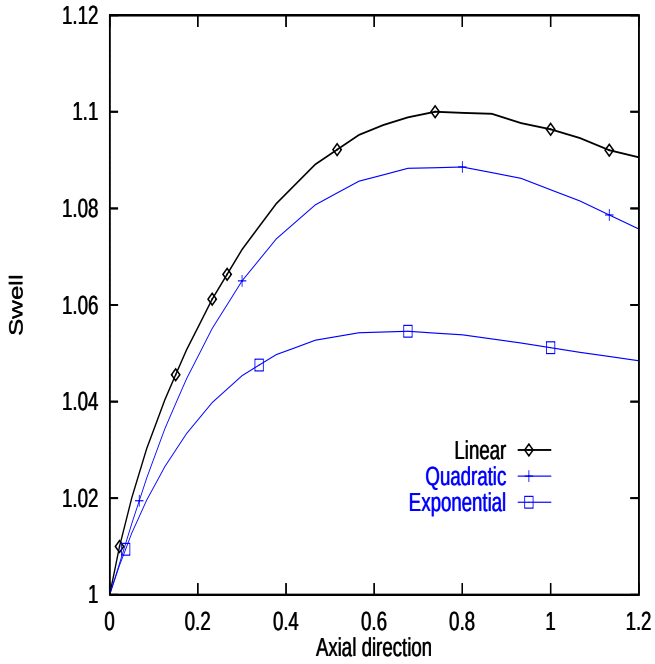

(c) **PTT(1,0,0.99), We=200**

Figure 12: **Short-die: PTT model, die swell on top free surface; variation with (a) We, (b) μ_1, (c) model**

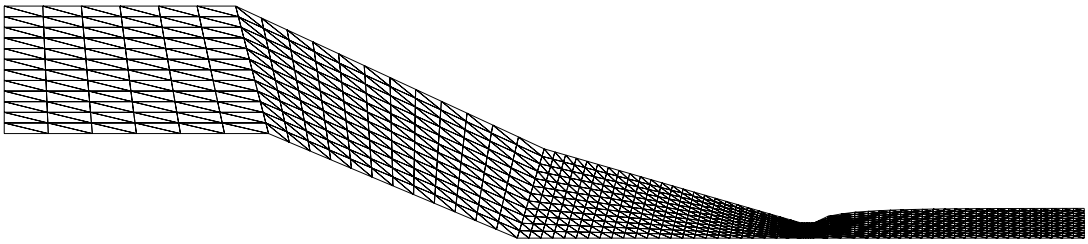

(a) **uniform mesh, 12×74 elements**

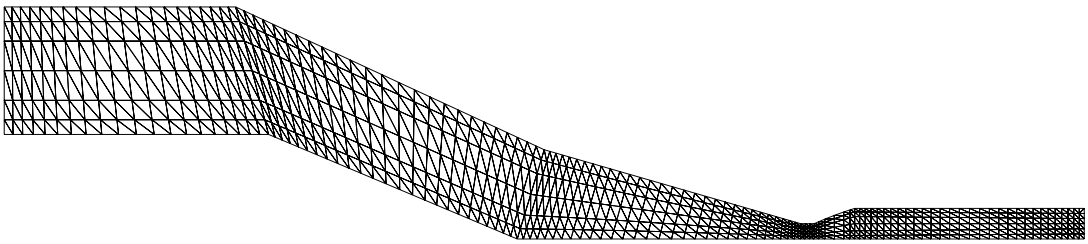

(b) **biased coarse mesh, 6×114 elements**

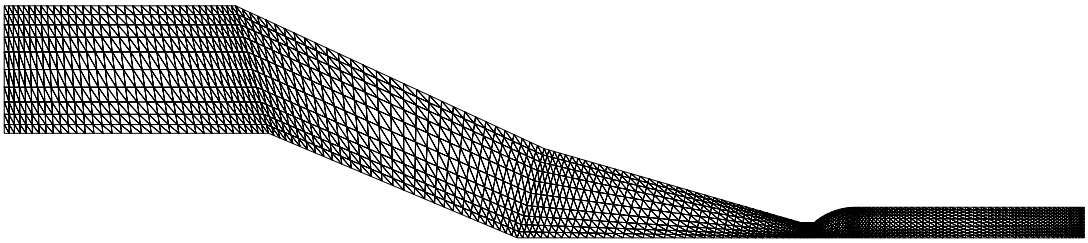

(c) **biased medium mesh, 10×168 elements**

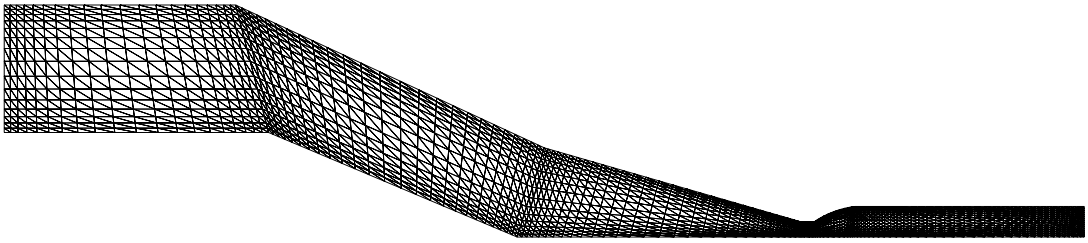

(d) **biased fine mesh, 15×127 elements**

Figure 13: **Full-die: mesh patterns**

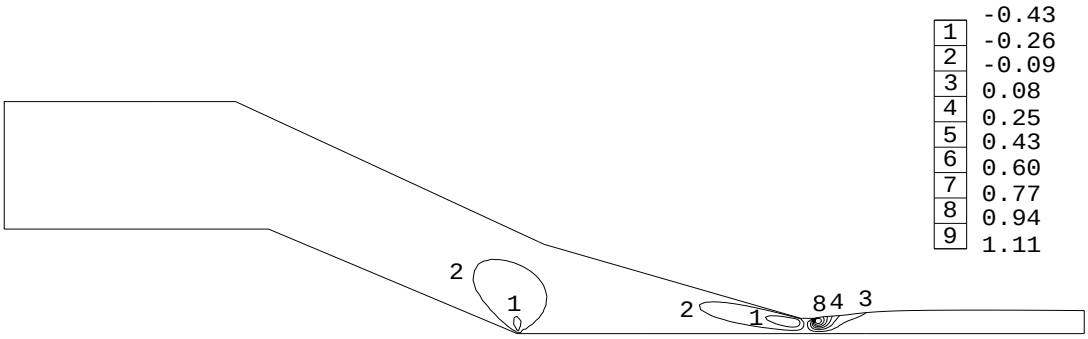

(a) V_r **contours**

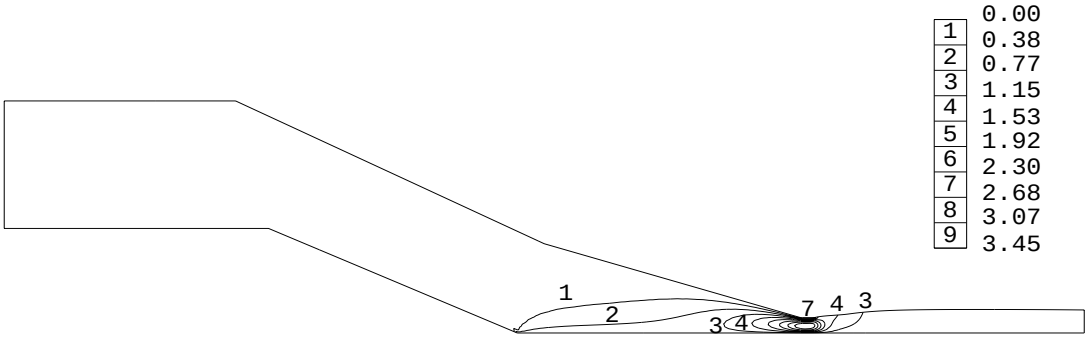

(b) V_z **contours**

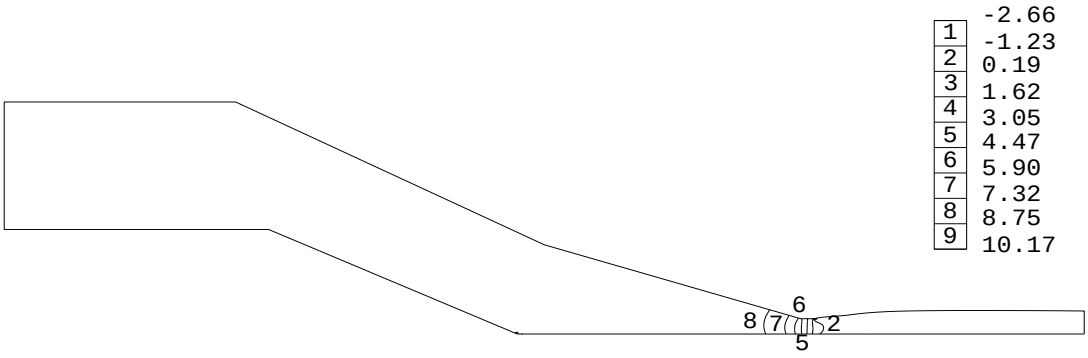

(c) **pressure contours**

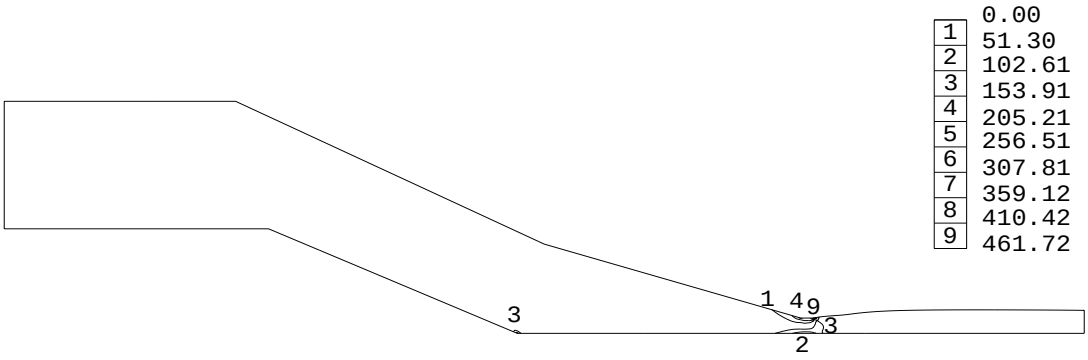

(d) I_2 **contours**

Figure 14: **Full-die: exponential PTT(1,0,0.99),** We**=200, biased fine mesh**

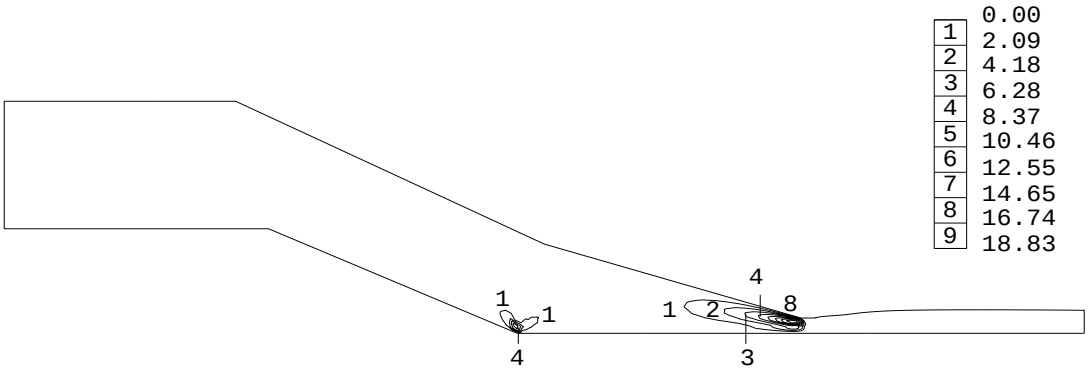

(e) $\dot{\epsilon}$ **contours**

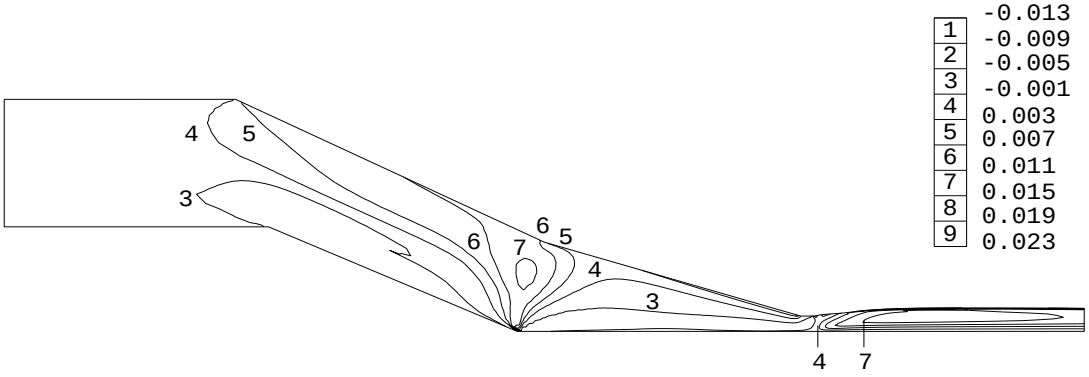

(f) T_{rr} **contours**

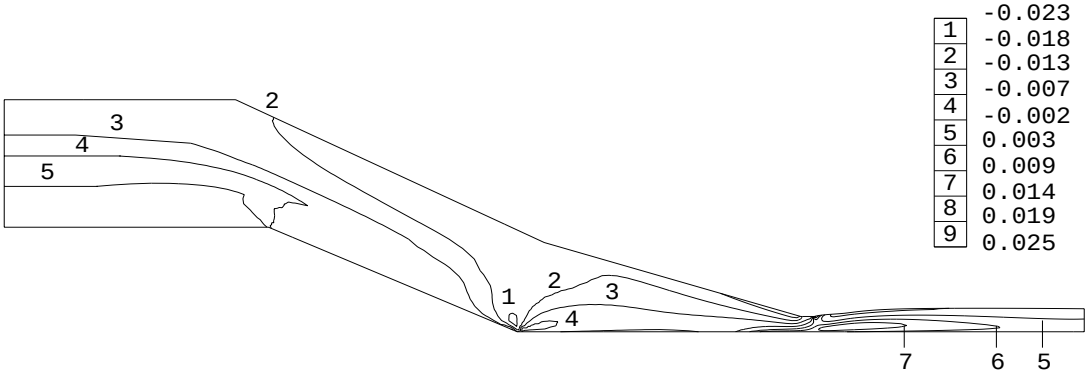

(g) T_{rz} **contours**

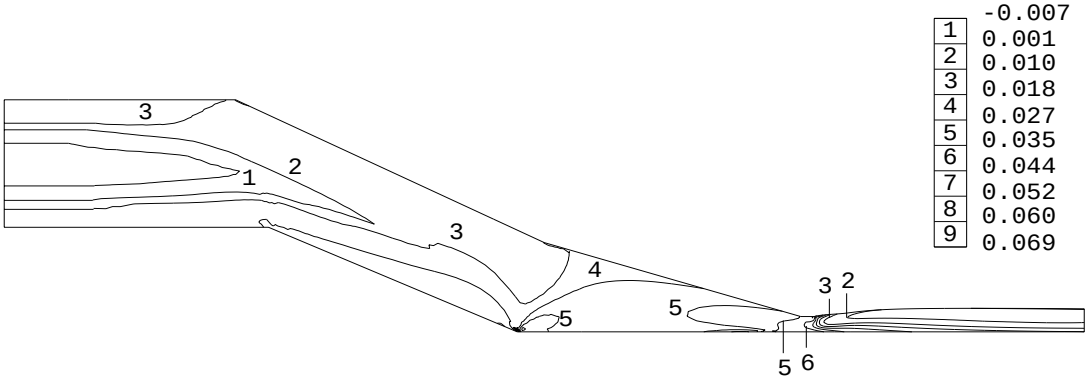

(h) T_{zz} **contours**

Figure 14: Continued **Full-die: exponential PTT(1,0,0.99)**, We**=200, biased fine mesh**

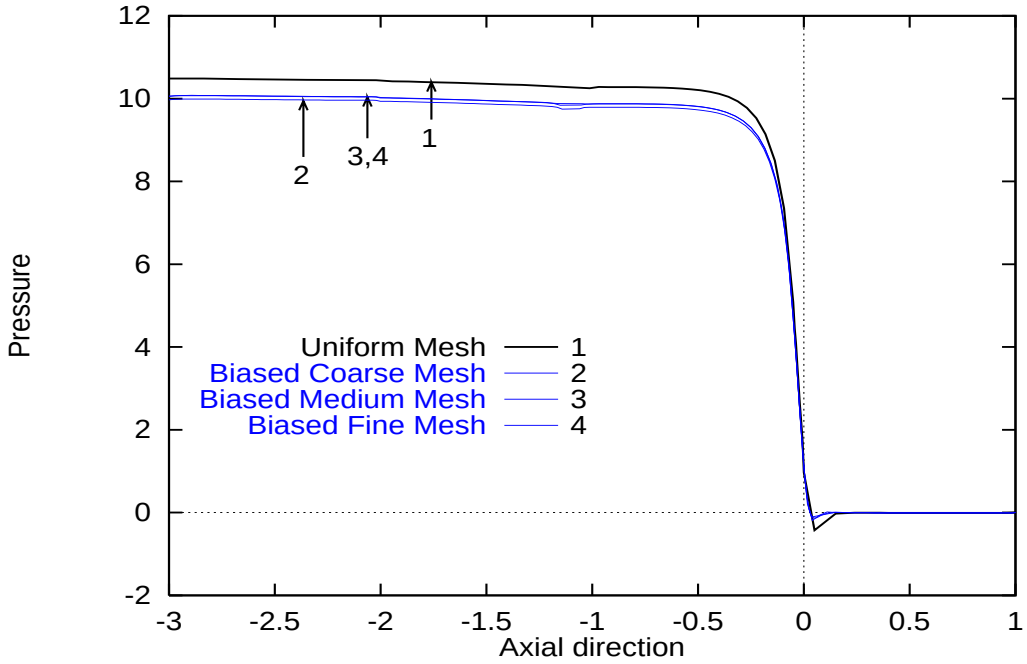

(a) **exponential PTT**

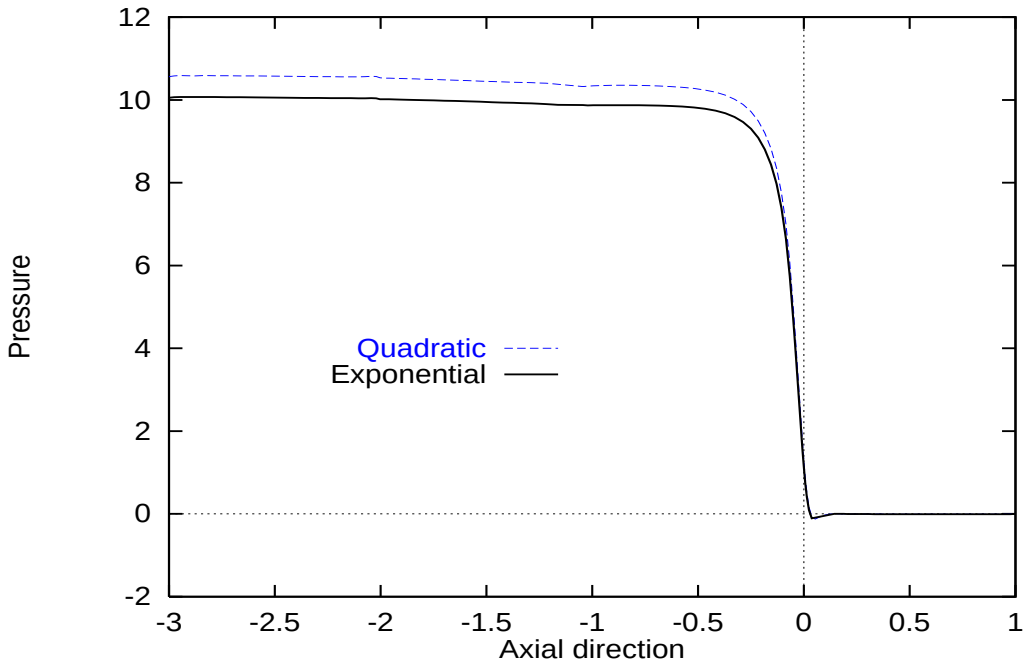

(b) **on biased fine mesh**

Figure 15: **Full-die: pressure on bottom surface**

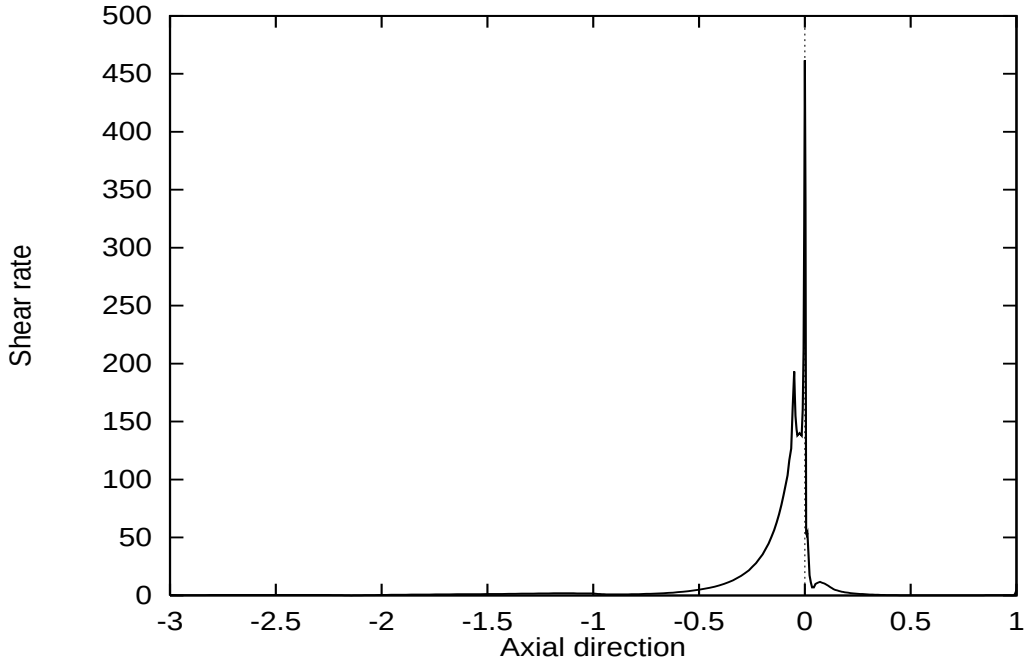

(a) **top surface**

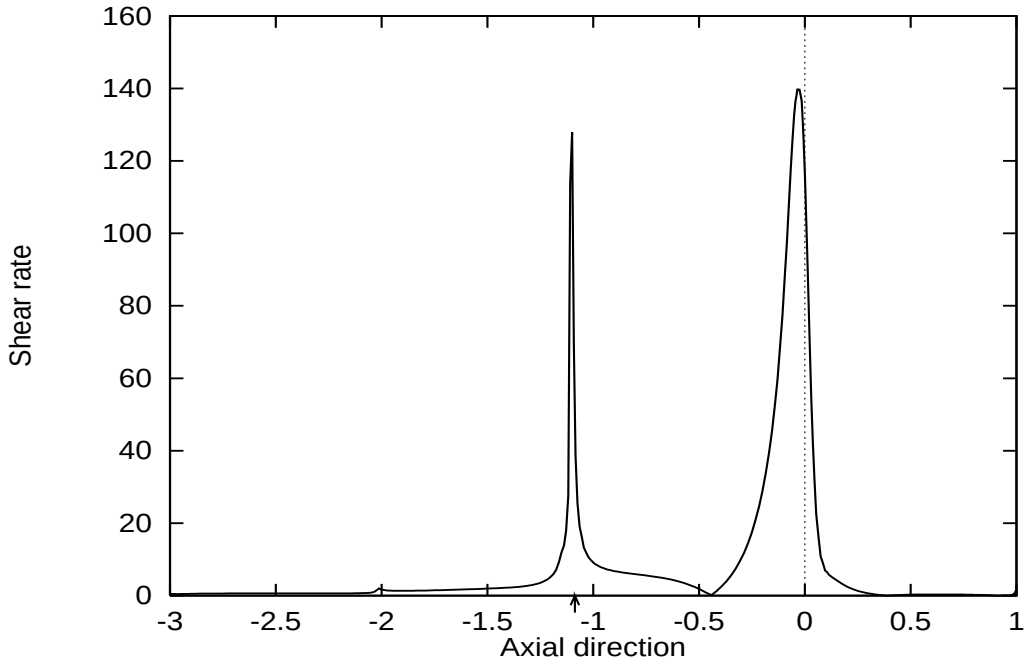

(b) **bottom surface**

Figure 16: **Full-die: I_2 on top and bottom surface, exponential PTT(1,0,0.99), biased fine mesh**

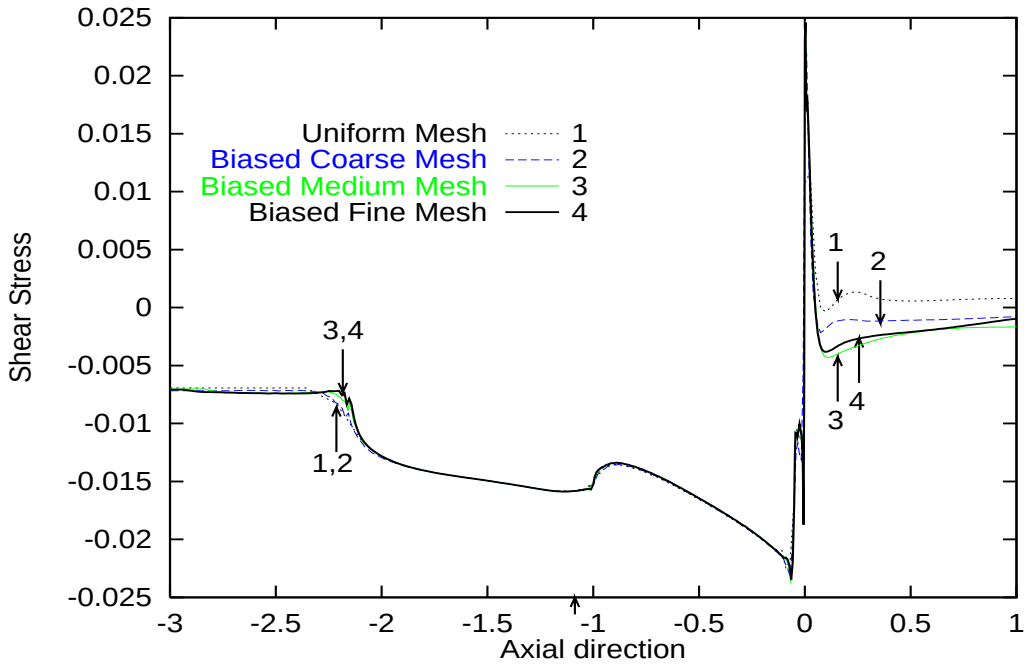

(a) **exponential PTT**

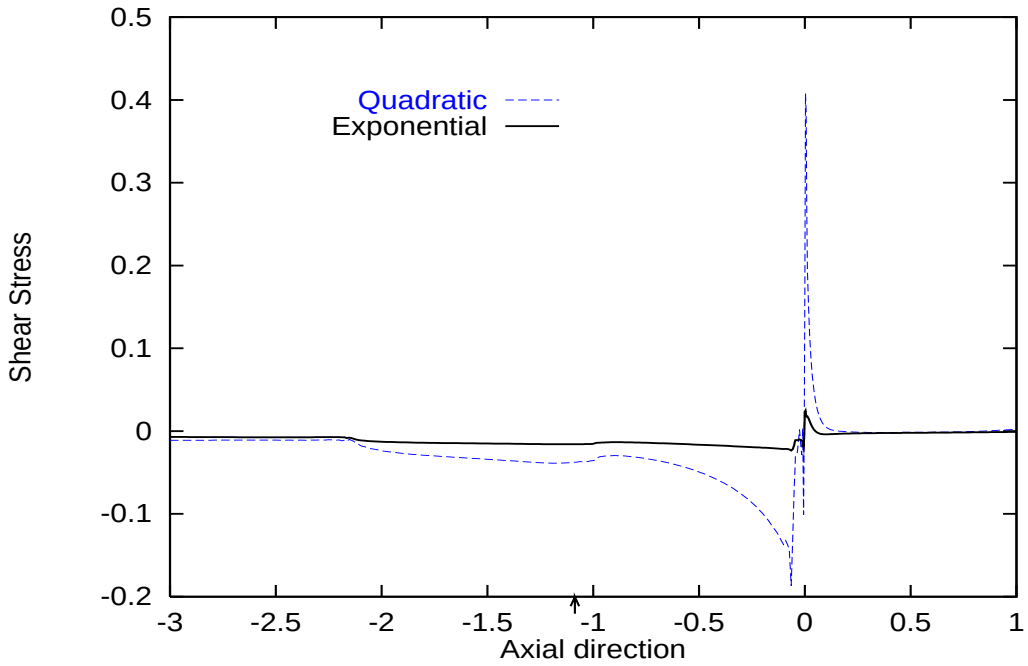

(b) **on biased fine mesh**

Figure 17: **Full-die: T_{rz} on top surface**

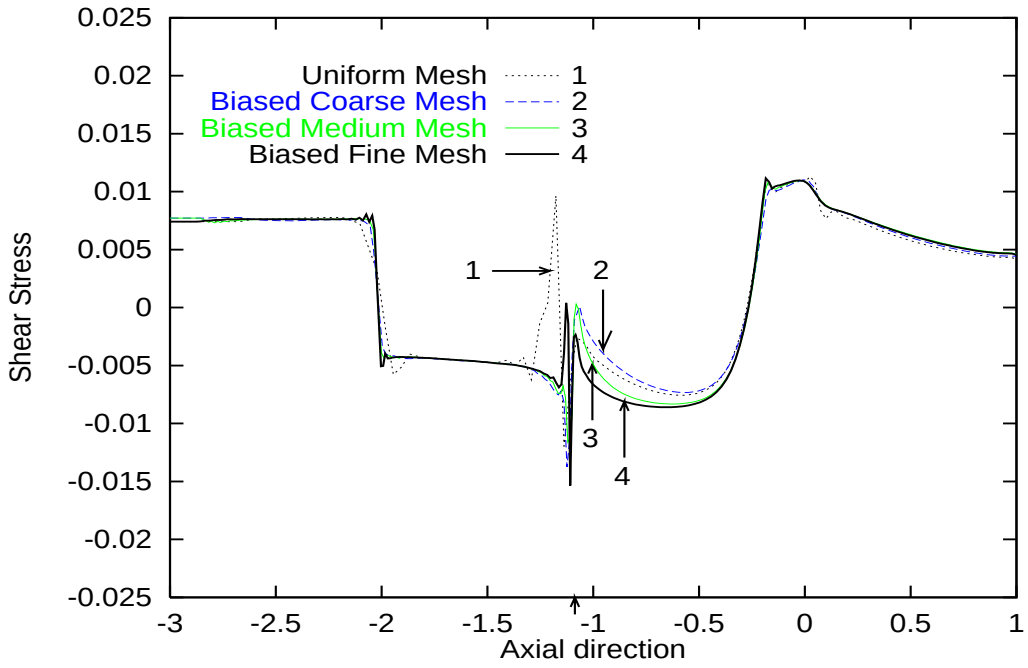

(a) **exponential PTT**

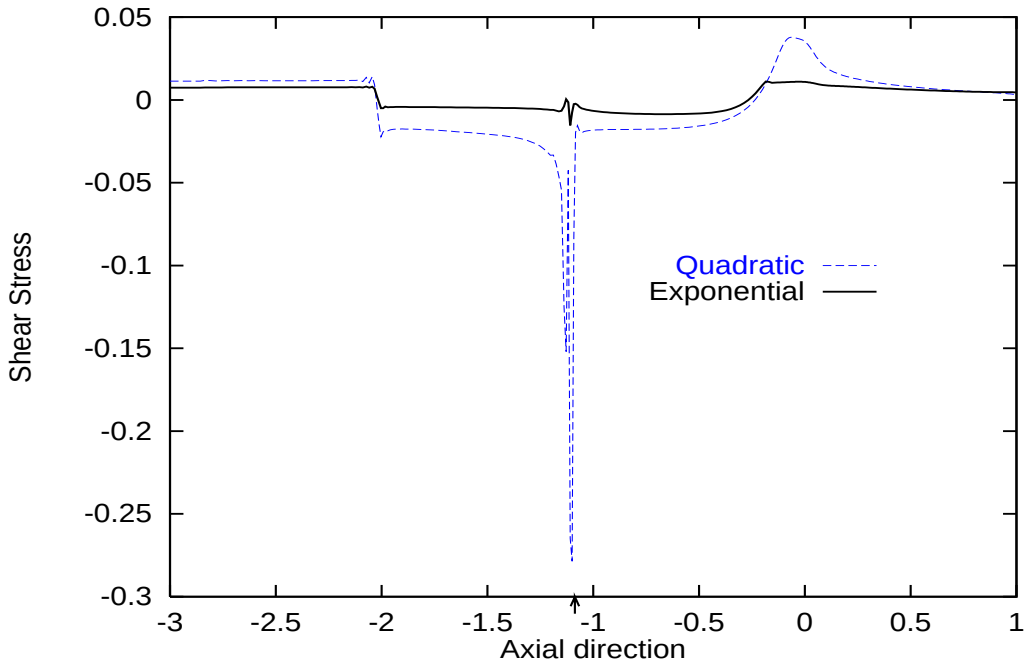

(b) **on biased fine mesh**

Figure 18: **Full-die: T_{rz} on bottom surface**

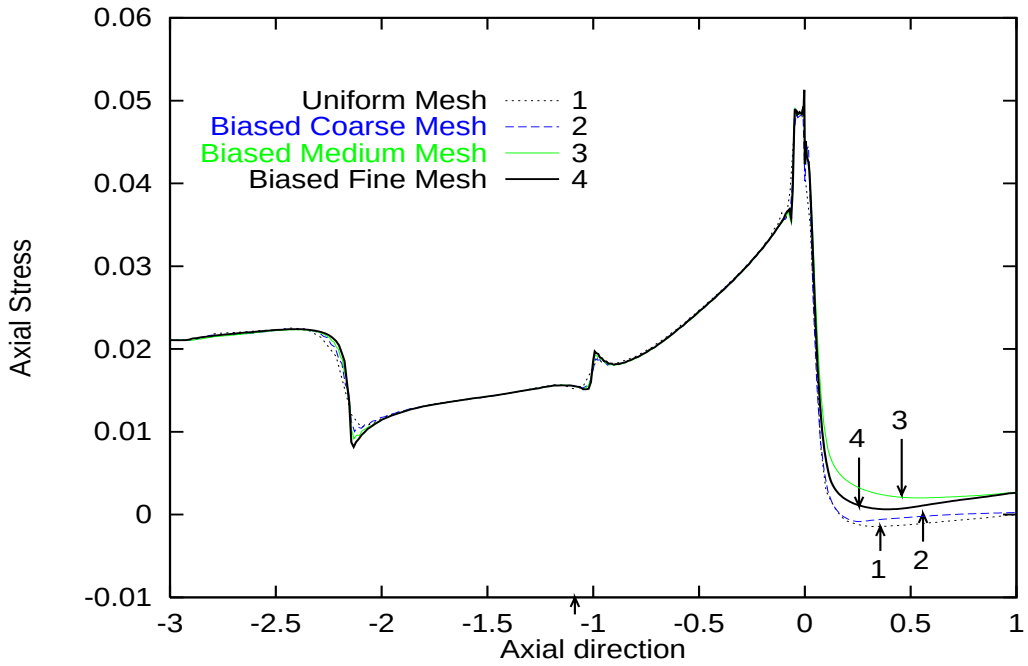

(a) **exponential PTT**

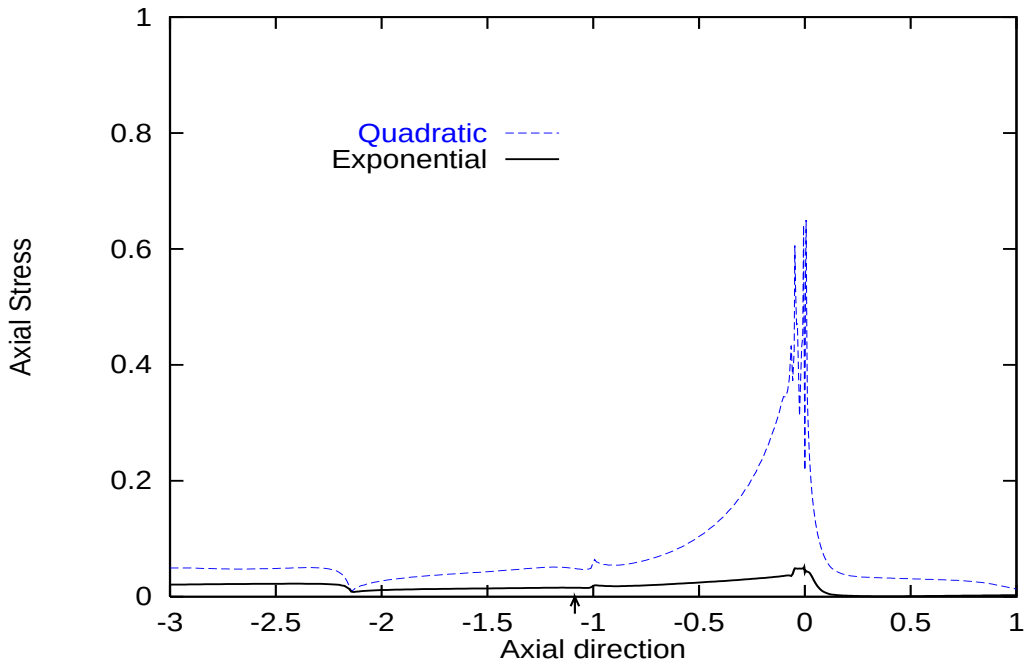

(b) **on biased fine mesh**

Figure 19: **Full-die: T_{zz} on top surface**

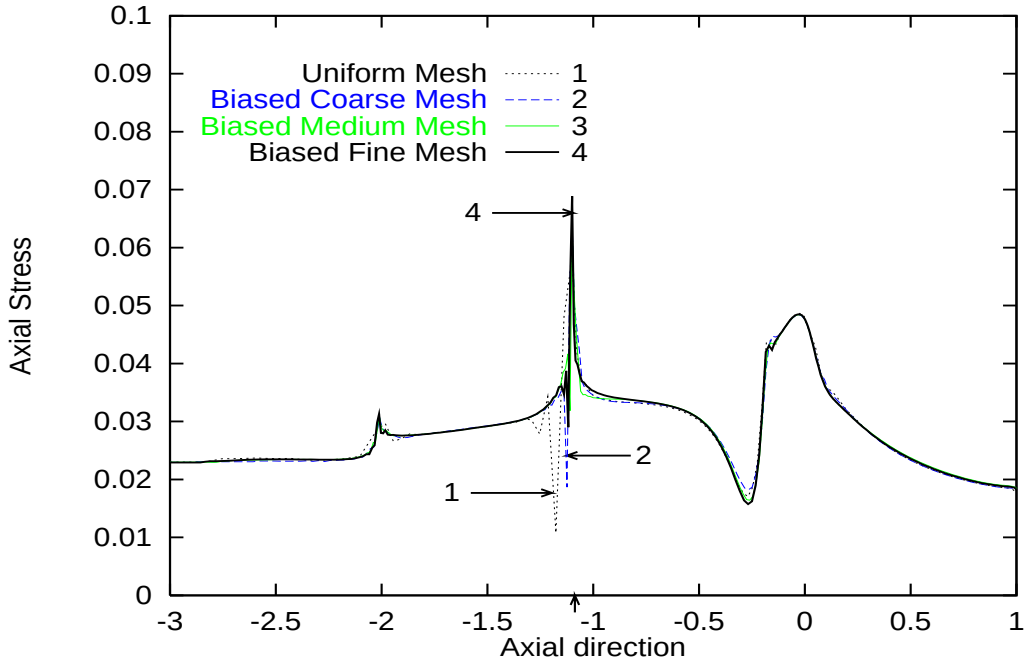

(a) **exponential PTT**

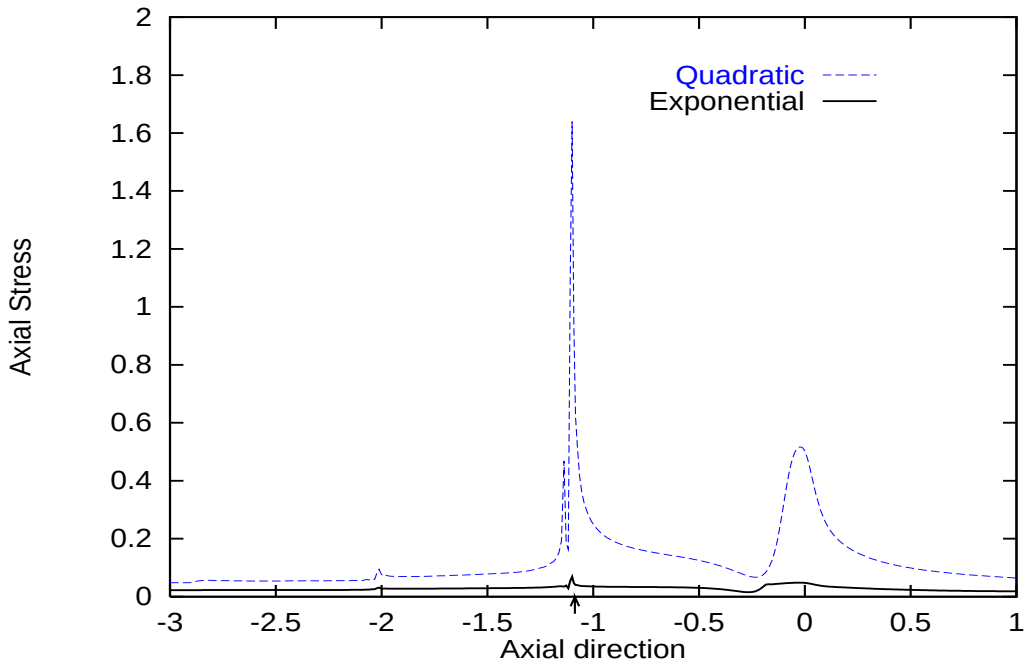

(b) **on biased fine mesh**

Figure 20: **Full-die: T_{zz} on bottom surface**

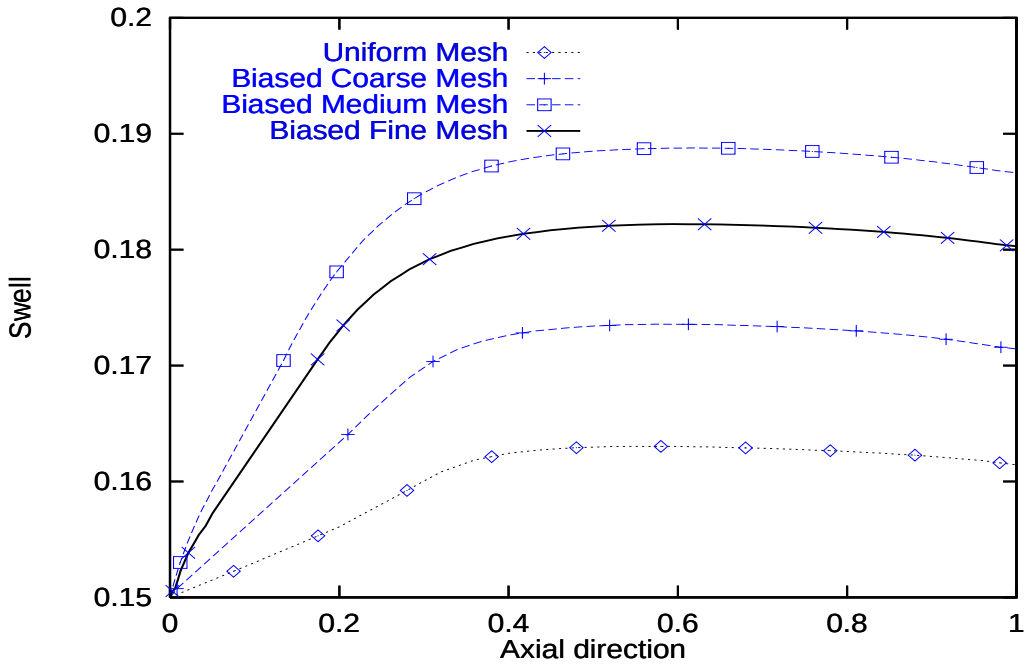

(a) **exponential PTT**

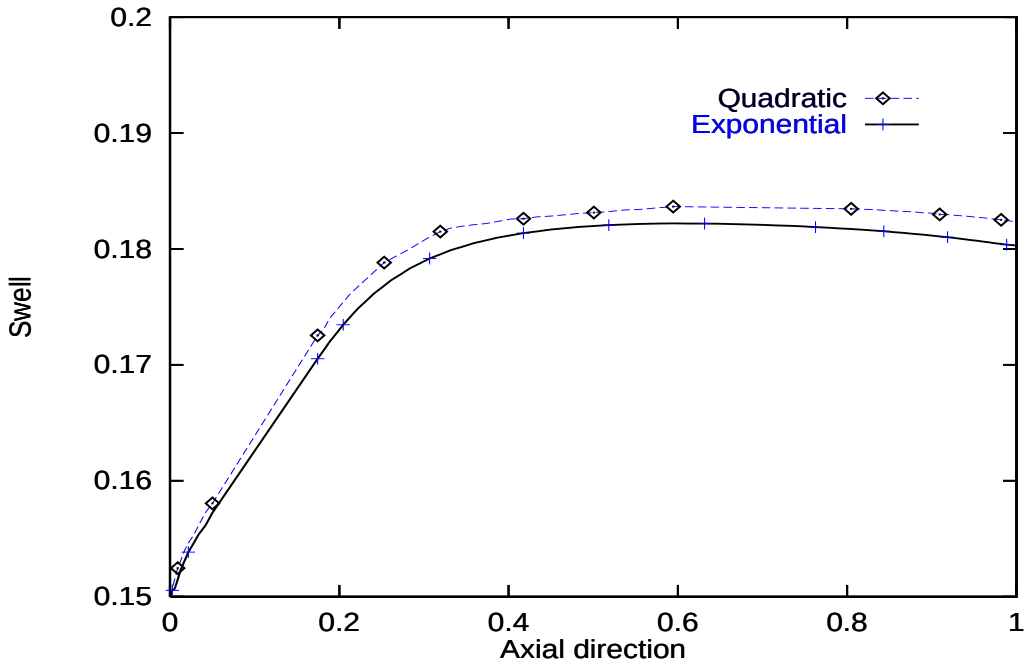

(b) **on biased fine mesh**

Figure 21: **Full-die: die swell on top free surface**